https://doi.org/10.5194/amt-2022-218
Preprint. Discussion started: 1 August 2022

Atmospheric Measurement Techniques Discussions

High Resolution 3D Winds Derived from a Newly Developed WISSDOM Synthesis Scheme using Multiple Doppler Lidars and Observations

Chia-Lun Tsai[1], Kwonil Kim[1], Yu-Chieng Liou[2], and Gyuwon Lee*[1]

[1]Department of Astronomy and Atmospheric Sciences, Center for Atmospheric REmote sensing (CARE), Kyungpook National University, Daegu, South Korea

[2]Department of Atmospheric Sciences, National Central University, Jhongli, Taiwan

* Corresponding author: Prof. Gyuwon Lee, E-mail: gyuwon@knu.ac.kr

https://doi.org/10.5194/amt-2022-218
Preprint. Discussion started: 1 August 2022

Abstract

A WISSDOM (Wind Synthesis System using Doppler Measurements) synthesis scheme was developed to derive high-resolution 3-dimensional (3D) winds under clear-air conditions. From this variational-based scheme, detailed wind information was obtained from scanning Doppler lidars, automatic weather stations (AWSs), sounding observations, and local reanalysis datasets (LDAPS, Local Data Assimilation and Prediction System), which were utilized as constraints to minimize the cost function. The objective of this study is to evaluate the performance and accuracy of derived 3D winds from this newly developed scheme. A strong wind event was selected to demonstrate its performance over complex terrain in Pyeongchang, South Korea. The size of the test domain is 12 × 12 km^2 extended up to 3 km height mean sea level (MSL) with remarkably high horizontal and vertical resolution of 50 m. The derived winds reveal that reasonable patterns were explored from a control run, as they have high similarity with the sounding observations. The results of intercomparisons show that the correlation coefficients between derived horizontal winds and sounding observations are 0.97 and 0.87 for u- and v-component winds, respectively, and the averaged bias (root mean square deviation, RMSD) of horizontal winds is between −0.78 and 0.09 (1.72 and 1.65) m s^{-1}. The correlation coefficients between WISSDOM-derived winds and lidar QVP (quasi-vertical profile) are 0.84 and 0.35 for u- and v-component winds, respectively, and the averaged bias (RMSD) of horizontal winds is between 2.83 and 2.26 (3.69 and 2.92) m s^{-1}. The statistical errors also reveal a satisfying performance of the retrieved 3D winds; the median values of wind directions are −5~5 (0~2.5) degrees, the wind speed is approximately −1~3 m s^{-1} (−1~0.5 m s^{-1}) and the vertical velocity is –0.2~0.6 m s^{-1} compared with the lidar QVP (sounding observations). A series of sensitivity tests with different weighting coefficients, radius of influence (RI) in interpolation and various combination of different datasets were also performed, and the results indicate that the present setting of the control run is the best reference to WISSDOM synthesis in this event.

https://doi.org/10.5194/amt-2022-218
Preprint. Discussion started: 1 August 2022

1. Introduction

In the past few decades, many practical methods have been developed to derive wind information by using meteorological radar data (Mohr and Miller, 1983, Lee et al., 1994, Liou and Chang, 2009, Bell et al. 2012). The derived winds substantially revealed reasonable patterns compared with conventional observations (such as surface stations, soundings, wind profiles, etc.) and models (Liou et al., 2014, North et al., 2017, Chen, 2019, Oue et al., 2019). Most comprehensive applications of the derived winds were adopted to document kinematic and precipitation structures associated with various weather systems at different scales (Yu and Tsai, 2013, Yu and Tsai, 2017, Tsai et al. 2018, Yu et al., 2020, Cha and Bell, 2021, Tsai et al., 2022). In addition, the accuracy of ~~3D~~ winds could be improved when increasing the number~~s~~ of Doppler radar because relatively fewer assumptions and more information can be included (Yu and Tsai 2010, Liou and Chang, 2009). Therefore, the retrieved schemes within multiple Doppler radars are a more popular way to obtain high-quality 3D winds and have been extensively applied to meteorological analyses.

The technique of velocity track display (VTD, Lee et al., 1994) and ground-based velocity track display (GBVTD, Lee et al., 1999) can derive the winds from single Doppler radar under some assumptions, as the wind patterns are generally uniform or axisymmetric rotational (Cha and Bell, 2021). More extended techniques based on VTD and GBVTD have also been applied to increase the quality of derived wind data, and such techniques include EGBVTD (Liou et al., 2006) and generalized velocity track display (GVTD, Jou et al., 2008). However, winds usually present nonuniform patterns and fast-evolving characteristics in most mesoscale weather systems and microscale phenomena, and complete and detailed winds are still difficult to resolve by these techniques. Instead of a single Doppler radar, multiple Doppler can retrieve better quality 3D winds with relativity fewer assumptions because they provide sufficient radial velocity measurements and wind information with wider coverage in the synthesis domain.

CEDRIC (Cartesian Space Editing, Synthesis, and Display of Radar Fields under Interactive

https://doi.org/10.5194/amt-2022-218
Preprint. Discussion started: 1 August 2022

Control, Mohr and Miller, 1983) is a traditional package used to retrieve 3D winds by dual-Doppler radar observations. This scheme usually determines the horizontal winds by using two radars, and the vertical velocity can be obtained by variational adjustment with anelastic continuity equation. Spline Analysis at Mesoscale Utilizing Radar and Aircraft Instrumentation (SAMURAI) software is another way to retrieve 3D winds (Bell et al., 2012); this scheme is a kind of variational data assimilation that adopts multiple radars. These two schemes were mainly developed by NCAR (National Center Atmospheric Research) and Colorado State University, and they are both open resources available on the websites of LROSE (Lidar Radar Open Software Environment, http://lrose.net and https://github.com/NCAR/lrose-cedric). Recently, Tsai et al. (2018) utilized the measurements of six Doppler radars to document precipitation and airflow structures over complex terrain on the northeastern coast of South Korea via WISSDOM (Wind Synthesis System using Doppler Measurements, Liou and Chang, 2009, Liou et al., 2012, Liou et al., 2016) ~~synthesis~~. Since one of the advantages of WISSDOM is that it considers the orographic forcing on Cartesian coordinates by applying IBM (immersed boundary method, Tseng and Ferziger, 2003), higher quality 3D winds can be derived well over terrain (Liou et al., 2013, 2014, Lee et al., 2018).

Generally, radial velocity is measured by detecting the movement of precipitation particles relative to the locations of Doppler radars; thus, there are no sufficient radial velocity measurements under clear-air conditions. However, the winds in clear-air conditions usually play an important role in the initiations of various weather systems and phenomena, such as downslope winds, gap winds, and wildfires (Reed, 1931, Colle and Mass, 2000, Mass and Ovens, 2019, Lee et al., 2020). Although surface stations, soundings, and wind profilers can measure winds under clear-air conditions, relatively poor spatial coverage is still a problem for obtaining sufficient wind information in certain local areas. Therefore, scanning Doppler lidars will be one approach to obtain wind information under clear-air conditions. Päschke et al. (2015) assessed the quality of wind derived by Doppler lidar with a wind profiler in a year trial, and the results showed good

https://doi.org/10.5194/amt-2022-218
Preprint. Discussion started: 1 August 2022

agreement in wind speed (the error ranged between 0.5 and 0.7 m s^{-1}) and wind direction (the error ranged between 5° and 10°). Bell et al. (2020) used an intersecting range height indicator (RHI) of six Doppler lidars to build "virtual towers" (such as wind profilers) to investigate the airflow over complex terrain during the Perdigão experiment. These virtual towers can fill the gap in wind measurements above conventional physical towers. The uncertainty of wind fields is also reduced by adopting multiple Doppler lidars (Choukulkar et al., 2017), and a high spatiotemporal resolution of derived wind is allowed to check small-scale rotors in mountainous areas (Hill et al., 2010).

The original WISSDOM was designed to retrieve 3D winds based on Doppler radar observations and background inputs combined with conventional observations and modeling. However, the original WISSDOM only provided 3D winds under precipitation conditions and not under clear-air conditions because the radar usually cannot detect radial velocity without precipitation particles. To obtain high-quality 3D winds under clear-air conditions, the radial velocity observed from the scanning Doppler lidars can be used in WISSDOM. Furthermore, the conventional observations and modeling datasets were used as isolated constraints in the modified WISSDOM synthesis scheme. One of the benefits of the isolated constraints is that it is easy to synthesize any kind of wind information obtained from available datasets and give suitable weighting coefficients with different constraints when they are processing the minimization in the cost function. Thus, more reliable 3D winds in clear-air conditions were well derived from this newly developed WISSDOM synthesis scheme.

The objective of this study is to modify the WISSDOM synthesis scheme based on the original version to be a more flexible and useful scheme by adding any number of Doppler lidars and conventional observations as well as modeling datasets. This newly developed WISSDOM will allow us to obtain an exceedingly high spatial resolution of 3D winds (50 m was set in this study) under clear- air conditions. A variety of adequate datasets were collected during a strong wind event in the winter season during an intensive field experiment ICE-POP 2018

https://doi.org/10.5194/amt-2022-218
Preprint. Discussion started: 1 August 2022

(International Collaborative Experiments for Pyeongchang 2018 Olympic and Paralympic winter games). In this study, detailed principles of the newly developed WISSDOM and data implementation are elucidated in the following sections. In addition, the newly developed WISSDOM was performed to retrieve 3D winds over complex terrain under clear-air conditions in a strong wind event. The reliability of the derived 3D winds was also evaluated with conventional observations.

2. Methodology

2.1 Original version of WISSDOM (WInd Synthesis System using DOppler Measurements)

WISSDOM is a mathematically variational-based scheme to minimize the cost function, and various wind-related observations can be used as one of the constraints in the cost function. The 3D winds were derived by variationally adjusted solutions to satisfy the constraints in the cost function. The original version of WISSDOM performed five constraints, including radar observations (i.e., reflectivity and radial velocity), background (combined with automatic weather stations, sounding, model or reanalysis data), continuity equation, vorticity equation, and Laplacian smoothing (Liou and Chang, 2009, Liou et al., 2012, Liou et al. 2016, Tsai et al., 2018). The cost function can be expressed as

$$J = \sum_{M=1}^{5} J_M \, , \tag{1}$$

where J_M is the different constraints. J_1 is the constraint related to the geometric relation between radar radial Doppler velocity observations (V_r) and derived one from true winds ($\mathbf{V}_t = u_t\mathbf{i} + v_t\mathbf{j} + w_t\mathbf{k}$) in Cartesian coordinates [eq. (2)].

$$J_1 = \sum_{t=1}^{2} \sum_{x,y,z} \sum_{i=1}^{N} \alpha_{1,i} \left(T_{1,i,t}\right)^2 . \tag{2}$$

https://doi.org/10.5194/amt-2022-218
Preprint. Discussion started: 1 August 2022

Since WISSDOM is a scheme that uses the 4DVAR approach, the variations between different time steps (t) should be considered, and two time (t) steps of radar observations were collected in this constraint. The x, y, z indicates the locations of a given grid point in the synthesis domain, and i could be any number (N) of radars (at least 1). The α_1 is the weighting coefficient of J_1 (α_2 is the weighting coefficient of J_2 and so on). $T_{1,i,t}$ in eq. (2) is defined as eq. (3):

$$T_{1,i,t} = (V_r)_{i,t} - \frac{(x - P_x^i)}{r_i} u_t - \frac{(y - P_y^i)}{r_i} v_t - \frac{(z - P_z^i)}{r_i} (w_t - W_{T,t}), \quad (3)$$

$(V_r)_{i,t}$ is the radial velocity observed by the radar (i) at time step (t), P_x^i, P_y^i and P_z^i depict the coordinate of radar i. The u_t, v_t and w_t ($W_{T,t}$) denote the 3D winds (terminal velocity of precipitation particles) at given grid points at the time step t; and $r_i = \sqrt{(x - P_x^i)^2 + (y - P_y^i)^2 + (z - P_z^i)^2}$.

The second constraint is the difference between the background ($\mathbf{V}_{B,t}$) and true (derived) wind field ($\mathbf{V}_t = u_t \mathbf{i} + v_t \mathbf{j} + w_t \mathbf{k}$), which is defined as

$$J_2 = \sum_{t=1}^{2} \sum_{x,y,z} \alpha_2 \left(\mathbf{V}_t - \mathbf{V}_{B,t}\right)^2. \quad (4)$$

There were several options to obtain background in the original version of WISSDOM. The most popular background resource involves using sounding observations; however, it can only provide homogeneous wind information for each level in WISSDOM with relatively coarse temporal resolution (3- to 12-hour intervals). The other option is combining sounding observations with AWS (automatic weather station) observations. Although the AWS provided wind information with better temporal resolution (1-min), the data were only observed at the surface layer with semirandom distributions. The last option is to combine sounding, AWS, modeling or reanalysis datasets. However, various datasets with different spatiotemporal resolutions are not favorable for appropriate interpolation of given grid points of WISSDOM synthesis, and the accuracy and reliability of the background may have been significantly affected by such a variety of datasets. Thus, these different observed or model data should be treated differently to minimize the

https://doi.org/10.5194/amt-2022-218
Preprint. Discussion started: 1 August 2022

Atmospheric Measurement Techniques Discussions

uncertainties and improve the accuracy. Thus, one of the improvements in the newly developed WISSDOM is that these inputs were separated into independent constraints individually. Note that the sounding observations are still a necessary dataset because the air density and temperature profile were used to identify the height of the melting level. In this study, sounding winds were adopted to represent the background for each level and a constraint at the same time; nevertheless, the AWS and reanalysis dataset are independent constraints in the newly developed WISSDOM (details are provided in the following section).

The third, fourth and fifth constraints in the cost function are the anelastic continuity equation, vertical vorticity equation and Laplacian smoothing filter, respectively. Equations (5), (6) and (7) are denoted as follows:

$$J_3 = \sum_{t=1}^{2} \sum_{x,y,z} \alpha_3 \left[\frac{\partial(\rho_0 u_t)}{\partial x} + \frac{\partial(\rho_0 v_t)}{\partial y} + \frac{\partial(\rho_0 w_t)}{\partial z} \right]^2, \quad (5)$$

$$J_4 = \sum_{x,y,z} \alpha_4 \left\{ \frac{\partial \zeta}{\partial t} + \left[u\frac{\partial \zeta}{\partial x} + v\frac{\partial \zeta}{\partial y} + w\frac{\partial \zeta}{\partial z} + (\zeta + f)\left(\frac{\partial u}{\partial x} + \frac{\partial v}{\partial y}\right) + \left(\frac{\partial w}{\partial x}\frac{\partial v}{\partial y} - \frac{\partial w}{\partial y}\frac{\partial u}{\partial z}\right) \right] \right\}^2, \quad (6)$$

$$J_5 = \sum_{t=1}^{2} \sum_{x,y,z} \alpha_5 [\nabla^2 (u_t + v_t + w_t)]^2. \quad (7)$$

ρ_0 in eq. (5) is the air density, and $\zeta = \partial v/\partial x - \partial u/\partial y$ in eq. (6).

2.2 The newly developed WISSDOM

In addition to the five constraints in the original version, the newly developed WISSDOM synthesis scheme includes three more constraints in the cost function. Thus, the cost function in the newly developed WISSDOM was written as

$$J = \sum_{M=1}^{8} J_M. \quad (8)$$

$J_1 \sim J_5$ in (8) are the same constraints corresponding to equations (2)-(7). The main purpose of this study is to retrieve 3D winds under clear-air conditions in which observational data are

https://doi.org/10.5194/amt-2022-218
Preprint. Discussion started: 1 August 2022

Atmospheric Measurement Techniques Discussions

relatively rare. Instead of the radial velocity $(V_r)_{i,t}$ observed from Doppler radars in eq. (3), the radial velocity observed from Doppler or wind lidars was adopted in the newly developed WISSDOM synthesis. In addition, if there were no precipitation particles under clear-air conditions, the terminal velocity of precipitation particles $(W_{T,t})$ was set to zero in eq. (3).

The sixth constraint is the difference between the derived wind fields and the sounding observations ($\mathbf{V}_{S,t}$), as defined in (9):

$$J_6 = \sum_{t=1}^{2} \sum_{x,y,z} \alpha_6 \left(V_t - V_{S,t}\right)^2. \tag{9}$$

The sounding data in J_6 were interpolated to the given grid points near its tracks bearing on the radius influence (RI) distance (the details are provided in Section 3.2.3). The main difference between J_6 and J_2 is that the sounding data were used as an observation for given 3D locations, instead of the constraint of homogeneous background winds for each level in the studied domain. The seventh constraint represents the discrepancy between the true (derived) wind fields and AWS ($\mathbf{V}_{A,t}$), as expressed in (8):

$$J_7 = \sum_{t=1}^{2} \sum_{x,y,z} \alpha_7 \left(V_t - V_{A,t}\right)^2. \tag{8}$$

Finally, the eighth constraint measures the misfit between the derived winds and the local reanalysis dataset ($\mathbf{V}_{L,t}$), as defined in (9):

$$J_8 = \sum_{t=1}^{2} \sum_{x,y,z} \alpha_8 \left(V_t - V_{L,t}\right)^2. \tag{9}$$

In this study, various observations and reanalysis datasets were utilized as constraints in the cost function of WISSDOM. The most important dataset is the radial velocity observed from Doppler lidars, which can measure wind information with high spatial resolution and good coverage from near the surface up to higher layers in the test domain. Sounding and AWS can provide horizontal winds for background or to be included in the constraints. The local reanalysis datasets were obtained from the 3DVAR LDAPS (Local Data Assimilation and Prediction System) data assimilation system from the KMA (Korea Meteorological Administration). Since these datasets have different coordinate systems and various spatiotemporal resolutions, additional procedures are required before the synthesis. Detailed descriptions of the procedures are described in the next section.

The high-quality synthesized 3D wind field from radar observations has been applied in several previous studies such as those by Liou and Chang (2009), Liou et al. (2012, 2013, 2014, 2016), and Lee et al. (2017). The advantages and details of the WISSDOM can be found in Tsai et al. (2018). This newly developed WISSDOM synthesis scheme has also been applied in the analysis related to the mechanisms of orographically induced strong wind on the northeastern coast of Korea (Tsai et al., 2022).

3. Data processing with a strong wind event

3.1 Basic information of WISSDOM synthesis

A small domain near the northeastern coast of South Korea was selected to derive detailed 3D winds over complex terrain (in the black box in the inset map in Fig. 1) because relatively dense and high-quality wind observations were only collected in this region during ICE-POP 2018. The size of the WISSDOM synthesis domain is 12 × 12 km^2 (up to 3 km MSL height) in the horizontal (vertical) direction with 50 m grid spacing. Such high spatial resolution 3D winds were synthesized every 1 hour in this test. Note that the output time steps are adjustable to be finer, but they are highly related to the temporal resolution of various datasets and computing resources. Two scanning Doppler lidars are located near the center of the domain: one is the equipped "WINDEX-2000" (the model's name from the manufacturer) at the MHS site, and the other is the "Stream line-XR" at the DGW site. In addition to the operational AWSs (727 stations), additional surface observations (32 stations) are also involved in ICE-POP 2018

https://doi.org/10.5194/amt-2022-218
Preprint. Discussion started: 1 August 2022

surrounding the MHS and DGW sites and the venues of the winter Olympic Games. The soundings are launched at the DGW site every 3 hours during the research period. The LDAPS also provided high spatial resolution of wind information in the test domain. The horizontal distribution of all instruments and datasets used are shown in Fig. 1.

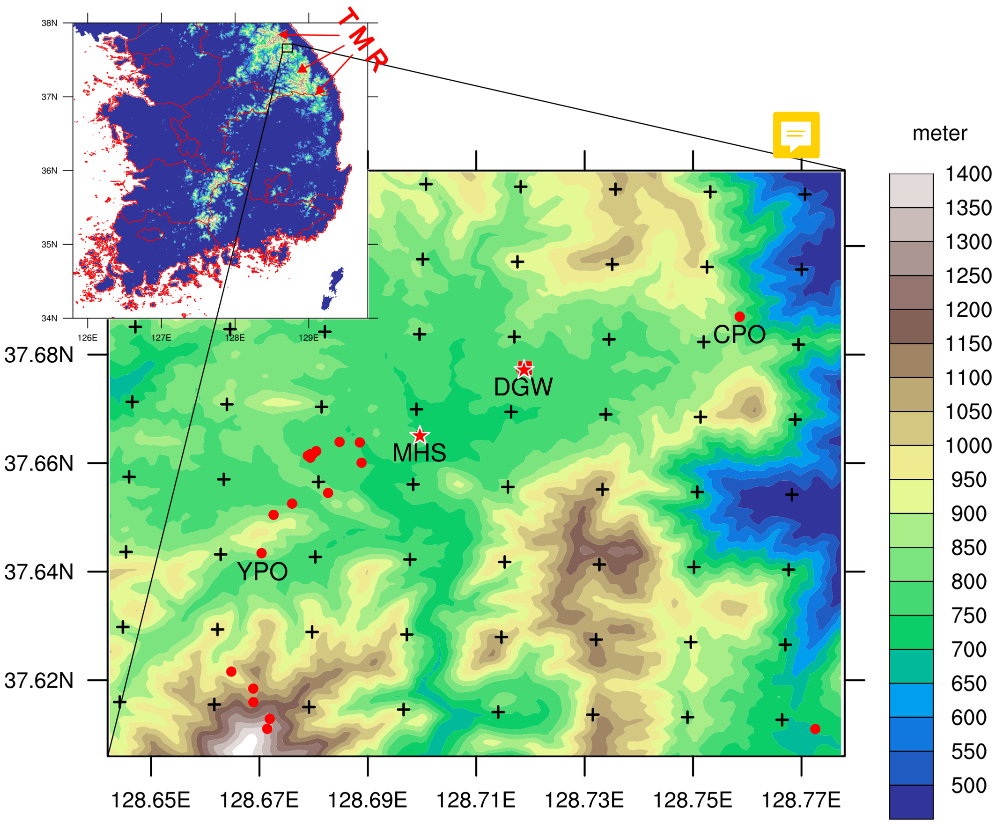

Figure 1. Horizontal distribution of instruments and datasets used in this study. A small box in the upper map indicates the WISSDOM synthesis domain. The Doppler lidars are marked by asterisks at the MHS and DGW sites. Red solid circles and squares indicate the automatic weather station (AWS) and sounding, respectively. The black cross marks the data points of LDAPS. Topographic features and elevations are shown with the color shading in a color bar in the figure. The location of the Teabeak Mountain Range (TMR) is also marked.

3.2 Data implemented in WISSDOM synthesis

3.2.1 Scanning Doppler lidars

The radial velocity observed from two scanning Doppler lidars was utilized to retrieve 3D

https://doi.org/10.5194/amt-2022-218
Preprint. Discussion started: 1 August 2022

winds via WISSDOM synthesis. The original coordinate system of observed lidar data is not a Cartesian coordinate system, but spherical (or polar) coordinate system. In the lidar data collection, the lasers were emitted from the transmitter with rotating azimuth angles at an initial elevation angle, and the scanner increased the elevation angles when surveillance (likely between 0° and 360° clockwise from north) or PPI (plan position indicator) was finished. The data were collected by raising the elevation angles until the expected maximum coverages were reached, which is called a volume scan. Consequently, the lidar repeated the surveillance from the initial to last elevation angles to complete the next volume scans. A complete hemispheric range height indicator (HRHI) or RHI demonstrated that the lidar finished a scan from 0° to 180° or from 0° to 90° at a fixed azimuth angle. Although relatively dense and complete coverage of wind information (i.e., radial velocity of aerosols) were sufficiently recorded by lidar observations, the collected data are usually not located directly on the given grid points in the WISSDOM synthesis (i.e., Cartesian coordinate system). In this study, the lidar data were interpreted simply from the lidar coordinate system to the Cartesian coordinate system via bilinear interpolation.

The scanning strategy of the lidar at the DGW site includes five elevation angles for PPI (7°, 15°, 30°, 45°, and 80° before 10:00 UTC on 14 Feb. 2018 and 4°, 8°, 14°, 25°, and 80° after 10:00 UTC) and two HRHIs at azimuth angles of 51° and 330°. A full volume scan included all PPIs and HRHIs every ~12 min. The maximum observed radius distance is ~13 km, and the grid spacing is 40 m for each gate along the lidar beam. The scanning strategy of the lidar at the MHS site involves seven elevation angles for PPI (5°, 7°, 10°, 15°, 30°, 45°, and 80°) and one HRHI at an azimuth angle of 0°. A full volume scan included all PPIs and RHIs every ~12 min. The maximum observed radius distance was ~8 km, and the grid spacing was 60 m. The vertical distribution of lidar data in the test domain is shown as blue lines in Fig. 2a.

3.2.2 Automatic weather station (AWS)

Most of the AWS stations are not exactly located on the given grid points of the Cartesian

https://doi.org/10.5194/amt-2022-218
Preprint. Discussion started: 1 August 2022

coordinate system. Objective analysis (Cressman, 1959) is a popular way to correct semirandom and inhomogeneous meteorological fields into regular grid points. This study adopted objective analysis for the AWS observations with adjustable RI distances between 100 m and 2000 m. After this first step, the observational data can reasonably interpolate to the given grid points horizontally. Furthermore, an additional step is required to put these interpolated data into the given grid points at different vertical levels because the AWSs are located at different elevations in the test domain. In the traditional way of original WISSDOM, the interpolated data are moved to the closest level with the shortest distance just above the AWS site. However, the interpolated data are NOT moved to the closest level if the shortest distances are large like more than half (50%) of gird spacing. Nevertheless, to include more data from the AWS observations appropriately, adjusted distances between the AWS sites and given grid points at different vertical levels were necessarily considered. These adjusted distances can be named as vertical extension (VE) here, and there are two options of 50% and 90% in the tests of this study, which correspond to 25 m and 45 m extensions between each grid (in case of the grid spacing is 50 m), respectively. An example demonstrated how to implement the interpolated data to the given grid points by adjustable VE after step one (Fig. 2b).

In Fig. 2b, the interpolated data do not need to move to a given grid point (as an example, at the 800 m level here) if the elevation of the AWS is equal to the height of a given grid point as point A. When the AWS is located higher than a given grid point (as point B in Fig. 2b) and does not reach the lower boundary of VE (50%) from the upper given grid point (i.e., at the 850 m level), this interpolated data will be removed and wasted. In contrast, when the interpolated data are located just below the given grid point with 50% VE, it will be achieved in the WISSDOM synthesis at the 800 m level (point C in Fig. 2b). The interpolated data of point D have a similar situation to point B; however, it will be achieved at the 800 m level because a higher VE (90%) was applied here. Since the locations of the AWS are semirandom with relatively sparse or concentrated distributions, the optimal RI and adjustable VE make it possible to include more

https://doi.org/10.5194/amt-2022-218
Preprint. Discussion started: 1 August 2022

307 AWS observations in the WISSDOM synthesis.

308

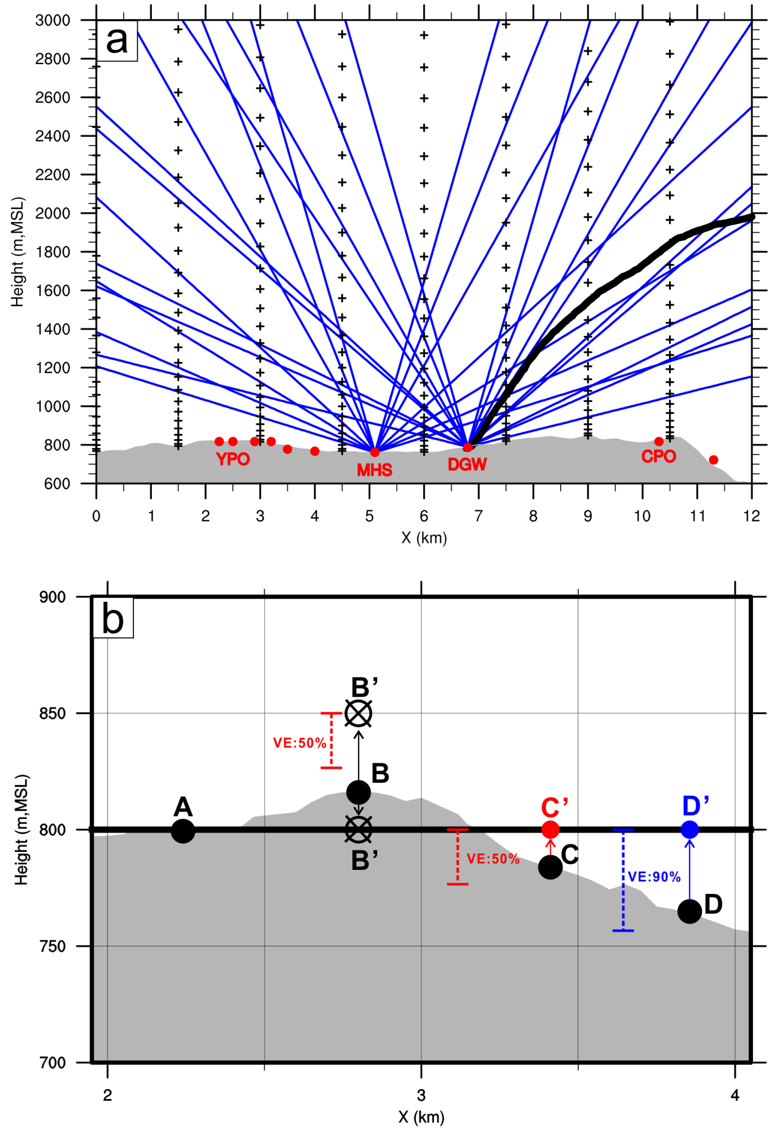

309

310 Figure 2. (a) Schematic diagram of the vertical distribution of adopted lidar datasets. Blue lines indicate the lidar

311 data observed at the DGW and MHS sites with different elevation angles. The AWS stations are located on the

312 ground and are marked by solid red circles. An example of a sounding track launched from the DGW site in one

313 time step (06:00 UTC on 14 Feb. 2018) is plotted as a thick black line. The black cross marks indicate the vertical

314 distribution of the LDAPS dataset. (b) Schematic diagram for data implementation with various locations of the

315 AWS stations and different percentages of VE (vertical extension) from given grid points at the 800 m MSL

316 level (thick black line). The gray shading on the bottom represents the topography.

https://doi.org/10.5194/amt-2022-218
Preprint. Discussion started: 1 August 2022

Atmospheric Measurement Techniques Discussions

3.2.3 Sounding

During ICE-POP 2018, the soundings are launched at the DGW site every 3 hours (from 00Z). Vertical profiles of air pressure, temperature, humidity, wind speed and directions were recorded every second (i.e., ~3 m vertical spatial resolution) associated with the rising sensor. The sounding sensor drifted when rising, and an example of its track in one time step is shown as a thick black line in Fig. 2a. In this example, the sounding movement was mostly affected by westerly winds, and it measured the meteorological parameters in any location along the track in the test domain. The coordinate system of sounding data is quite similar to the distribution of AWS measurements, and the observations are not located right on the given grid points of the WISSDOM synthesis.

Similar to the AWS data, the sounding data also underwent objective analysis with an adjustable RI distance for the wind measurements in the first step. Then, the interpolated data were switched to given grid points for each vertical level by the different VE in the WISSDOM synthesis.

3.2.4 Reanalysis dataset: LDAPS

The local reanalysis dataset LDAPS was generated by the KMA. This dataset provides u- and v-component winds every 3 hours, and the horizontal spatial resolution is ~1.5 km with the grid type in Lambert Conformal (as black cross marks in Fig. 1). The data revealed denser distributions near the surface and sparse distributions at higher levels (see Fig. 2a). The initiations of wind variables in the LDAPS were assimilated with many observational platforms, including radar, AWS, satellite and sounding data. Thus, the relatively high reliability of this dataset could be expected. In addition, such datasets have also significantly improved the forecast ability in small-scale weather phenomena over complex terrain in Korea (Kim et al., 2019, Choi et al., 2020, Kim et al., 2020).

https://doi.org/10.5194/amt-2022-218
Preprint. Discussion started: 1 August 2022

The LDAPS data are not located directly on the given grid points of the WISSDOM synthesis system. Unlike the distribution of AWS and sounding observations, LDAPS has dense and good coverage in the test domain. Therefore, like lidar observations, the LDAPS data were also interpolated to the given grid points on the Cartesian coordinate system via the bilinear interpolation method.

3.3 Overview of the selected strong wind event

A strong wind event was selected to evaluate the performance of this newly developed WISSDOM synthesis scheme. In this strong wind event, the evolution of surface wind patterns on the Korean Peninsula was mainly dominated by a moving low-pressure system (LPS) which is one type of strong downslope winds (Park et al, 2022, Tsai et al., 2022). The LPS moved out from China and penetrated the northern part of the Korean Peninsula through the Yellow Sea beginning at approximately 12:00 UTC on 13 February 2018. Consequently, a relatively strong surface wind speed (exceeding ~17 m s^{-1}) was observed when the LPS was located near the northeastern coast of the Korean Peninsula (~130°E, 40°N) at 00:00 UTC on 14 February 2018 (Fig. 3). Then, the surface wind speed became weak when the LPS moved away from South Korea after 00:00 UTC on 15 February 2018 (not shown); the details of the synoptic conditions can be found in Tsai et al. (2022).

https://doi.org/10.5194/amt-2022-218
Preprint. Discussion started: 1 August 2022

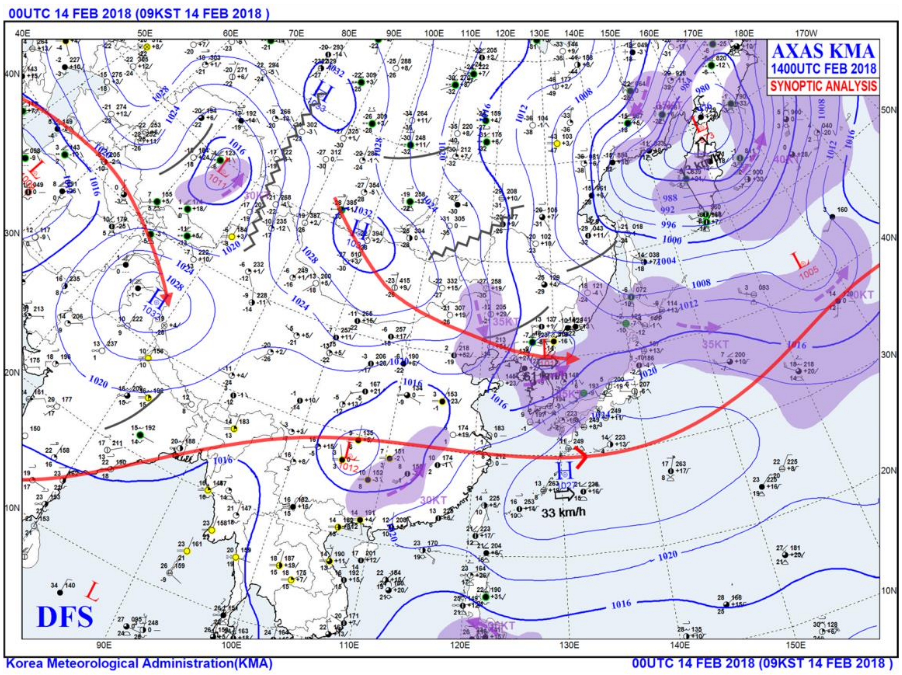

Figure 3. Synoptic surface chart from the Korea Meteorological Administration (KMA) at 00:00 UTC on 14 Feb. 2018.

This event is one of two strong wind events (i.e., daily maximum wind speeds larger than 10 m s^{-1} observed at the AWS sites along the northeastern coast of South Korea) in the past decade based on the KMA historic record. Such a strong wind event may help us to examine the potential maximum errors of the retrieved winds. Since persistent, strong westerly winds were observed by the soundings and AWS from near the surface and upper layers over the TMR during the event, the data coverages in the test domain were checked during a chosen time step (06:00 UTC on 14 February 2018). The percentage of data occupations for each dataset (after interpolation) was checked, and the results are shown in Fig. 4. Note that the elevation of the TMR is approximately 700 m MSL in the test domain. The lidars provided good coverage of 100% to 50% at the lower layers between 700 m and 800 m MSL. The coverage of lidars was reduced significantly above 900 m MSL and remained at ~5%. The maximum coverage of the AWS observations is ~40% at 800 m, and there was less coverage above this layer since relatively

https://doi.org/10.5194/amt-2022-218
Preprint. Discussion started: 1 August 2022

few AWS stations are located in the higher mountains. Because only one sounding observation was utilized in this domain, relatively few coverages were also depicted. The local reanalysis LDAPS can provide complete coverage above 900 m MSL (exceeding 100%), albeit there was less coverage in the lower layers due to terrain. The lidar, sounding, and AWS observations covered most areas at lower levels but not higher levels; thus, the LDAPS compensated for most of the wind information at the upper layers in the WISSDOM synthesis.

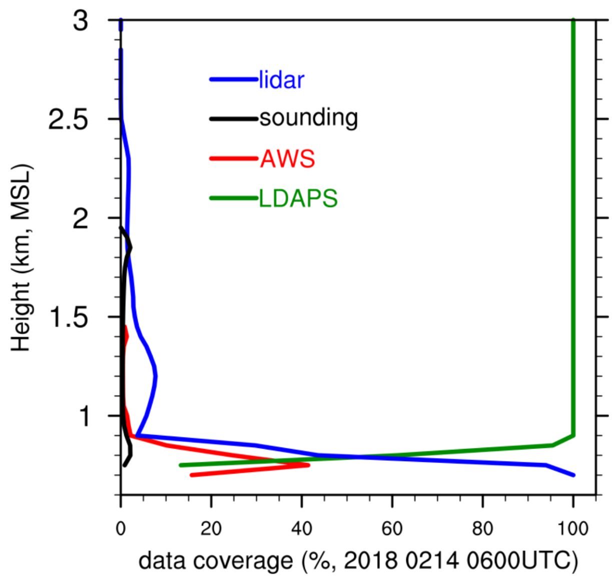

Figure 4. Data coverage (percentage, %) of the lidar (blue line), sounding (black line), AWS (red line) observations, and LDAPS (green line) at 06:00 UTC on 14 Feb. 2018.

4. Control run and the accuracy of WISSDOM

4.1 Control run

Relatively reliable 3D winds were derived by a control run of the WISSDOM synthesis because all available wind observations and local reanalysis datasets were fully acquired. These datasets provided sufficient and complete wind information with a high percentage of coverage in the test domain (cf. Fig. 4). The control run was performed carefully with the necessary

https://doi.org/10.5194/amt-2022-218
Preprint. Discussion started: 1 August 2022

Atmospheric Measurement Techniques Discussions

procedures in data implementation before running the WISSDOM synthesis. The lidar and LDAPS datasets must perform bilinear interpolation to the given grid points in WISSDOM, and the sounding and AWS observations must undergo objective analysis with the appropriate RI distance and VE. The quantities of the weighting coefficients for each input dataset followed the default setting from the original version of WISSDOM. The 3D winds were derived during one time step at 06:00 UTC on 14 Feb. 2018 and compared with conventional observations. The basic setting of this control run is summarized in Table 1.

Table 1 Basic setting of WISSDOM (control run)

Domain Range	Latitude: 37.606°N~37.713°N Longitude: 128.642°E~128.778°E
Domain Size	12 × 12 × 3 km (long × width × vertical)
Spatial Resolution	0.05 × 0.05 × 0.05 km (long × width × vertical)
Terrain Resolution	0.09 km
Coordinate System	Cartesian coordinate system
Background	Sounding (DGW)
Data Implementation	Doppler Lidars (MHS, DGW): bilinear interpolation AWS: objective analysis (RI*: 1 km, VE*: 90%) Sounding (DGW): objective analysis (RI: 1 km, VE: 90%) LDAPS: bilinear interpolation
Weighting Coefficient (input datasets)	Doppler Lidars (α_1): 10^6 Background (α_2): 10^2 Sounding (α_6): 10^6 AWS (α_7): 10^6 LDAPS (α_8): 10^3

*RI: radius influence, VE: vertical extension

The results of 3D winds at 800 m MSL derived from the control run are shown in Figs. 5a, c, and e. Topographic features comprised relatively lower elevations in the center of the test domain, and there were weaker u-component winds (~7 m s^{-1}) near the AWSs and MHS lidar sites between 128.67°E and 128.71°E (Fig. 5a). In contrast, the u-component winds (~15 m s^{-1}) were almost doubled near the DGW lidar site (between 128.71°E and 128.73°E). The vertical structures of the u-component winds across these two lidars (i.e., along the black line in Fig. 5a)

https://doi.org/10.5194/amt-2022-218
Preprint. Discussion started: 1 August 2022

Atmospheric Measurement Techniques Discussions

are shown in Fig. 5b. The strength of the u-component winds rapidly increased from the surface to the upper layers (from ~6 to 20 m s^{-1}), and uniform u-component winds with wavy pattern were depicted above ~1 km MSL except for the stronger winds near the surface surrounding the DGW site. There were relatively weak (strong) u-component winds surrounding the lidar at the MHS (DGW) site near the surface. Relatively weak v-component winds were found (approximately ±4 m s^{-1}) at 800 m MSL (Fig. 5c); thus, the horizontal wind directions were mostly westerly winds during this time step. The v-component winds were obviously accelerated in several local areas encompassing the terrain (near 128.71°E). The vertical structure of the v-component winds (Fig. 5d) indicates that the v-component winds became stronger in the upper layer. The wind directions were changed from westerly to southwesterly from the near surface up to ~1.4 km MSL height. Updrafts were triggered on windward slopes when westerly winds impinge the terrain or hills (Figs. 5e and 5f). Basically, the 3D winds derived from the WISSDOM synthesis reveal reasonable patterns compared to synoptic environmental conditions (cf. Fig. 3); the moving LPS accompanied stronger westerly winds.

https://doi.org/10.5194/amt-2022-218
Preprint. Discussion started: 1 August 2022

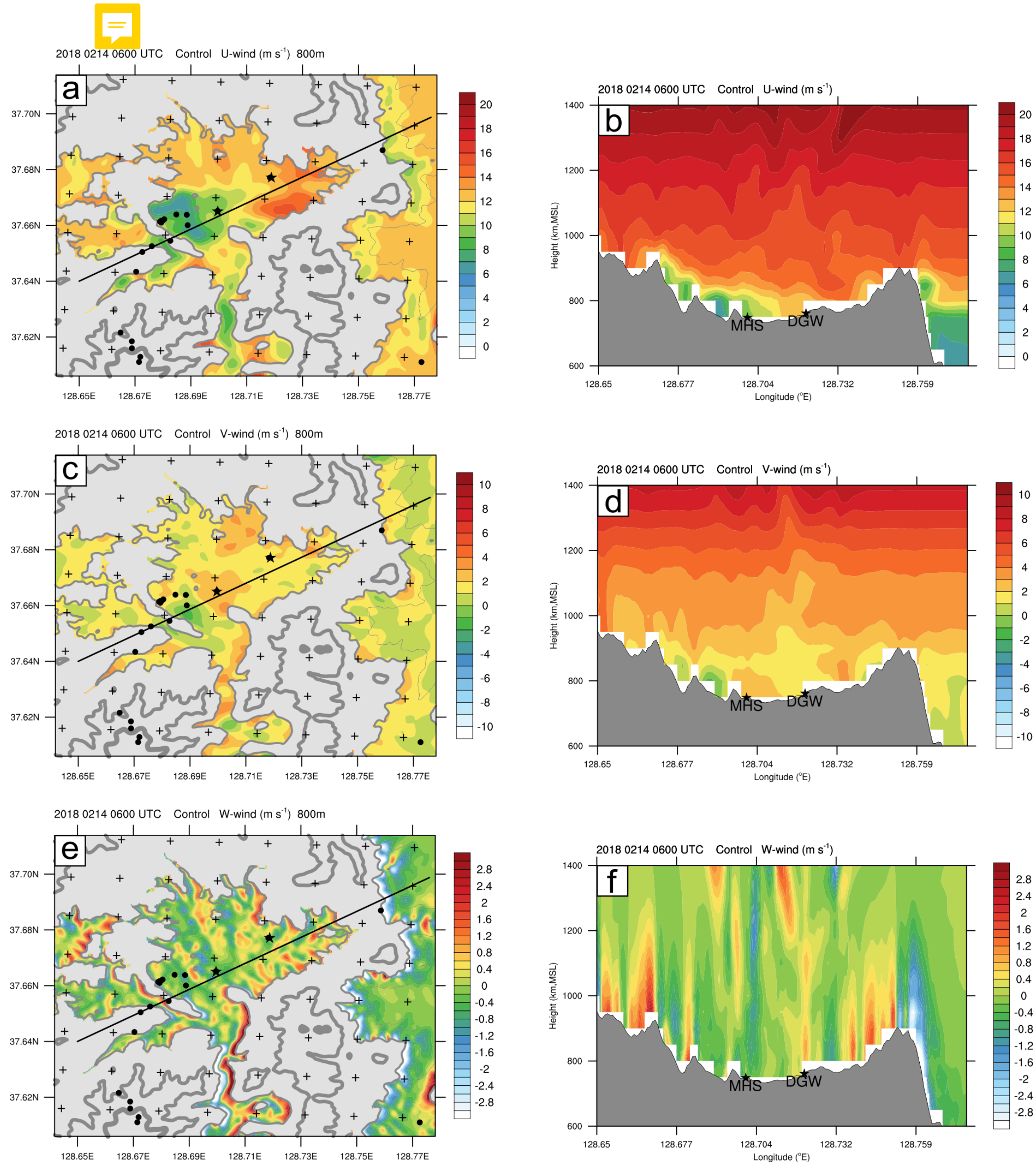

Figure 5. The 3D winds were derived from the control run by the WISSDOM synthesis at 06:00 UTC on 14 Feb. 2018. (a) The u-component winds (color, m s^{-1}) at 800 m MSL; the gray shading represents the terrain area, and the contours indicate different terrain heights of 600 m, 800 m and 1000 m MSL corresponding to thin to thick contours. The locations of lidars are marked with asterisks. (b) Vertical structures of u-component winds (color, m s^{-1}) along the black line in (a) The gray shading in the lower part of the figure indicates the height of the terrain. (c) and (d) are the same as (a) and (b) but for the v-component winds. (e) and (f) are the same as (a) and (b) but for the w-component winds.

https://doi.org/10.5194/amt-2022-218
Preprint. Discussion started: 1 August 2022

Atmospheric Measurement Techniques Discussions

4.2 Intercomparison between derived winds and observations

Detailed analyses were performed in this section to quantitatively evaluate the accuracy of the derived 3D wind from the WISSDOM synthesis. Two kinds of instruments were available in the test domain to detect the relatively realistic winds: sounding and lidar quasi-vertical profiles (QVP, Ryzhkov et al., 2016). The horizontal winds observed from soundings and the 3D winds of the lidar QVP were utilized to represent observations. A complete analysis of the intercomparison between the WISSDOM synthesis and observations is presented in the following subsections.

4.2.1 Sounding

The discrepancies in horizontal winds derived from WISSDOM and the sounding observations for the entire research period (from 12:00 UTC on 13 to 12:00 UTC on 14 February 2018) were analyzed. Fig. 6 shows the scatter plots of the u- and v-component winds on the locations following the tracks of sounding launched from the DGW site. Most of the u-component winds derived from WISSDOM are in good agreement with the sounding observations, and the wind speed is increased with the height from approximately 10 to 40 m s^{-1}. Slight underestimation of retrieved u-component winds can be found at the layers of 1.5~2 km MSL (Fig. 6a). In contrast, most of the v-component winds were weak (smaller than 15 m s^{-1}) at all layers, because the environmental winds were more like westerlies during the research period. There were also slightly overestimated v-component winds derived from WISSDOM at the layers of 1.5~2 km MSL (Fig. 6b). The possible reason why the overestimated winds occurred above ~1.5 km MSL is that lidar data had relatively less coverages at higher layers (cf. Fig. 4).

https://doi.org/10.5194/amt-2022-218
Preprint. Discussion started: 1 August 2022

Atmospheric Measurement Techniques
Discussions

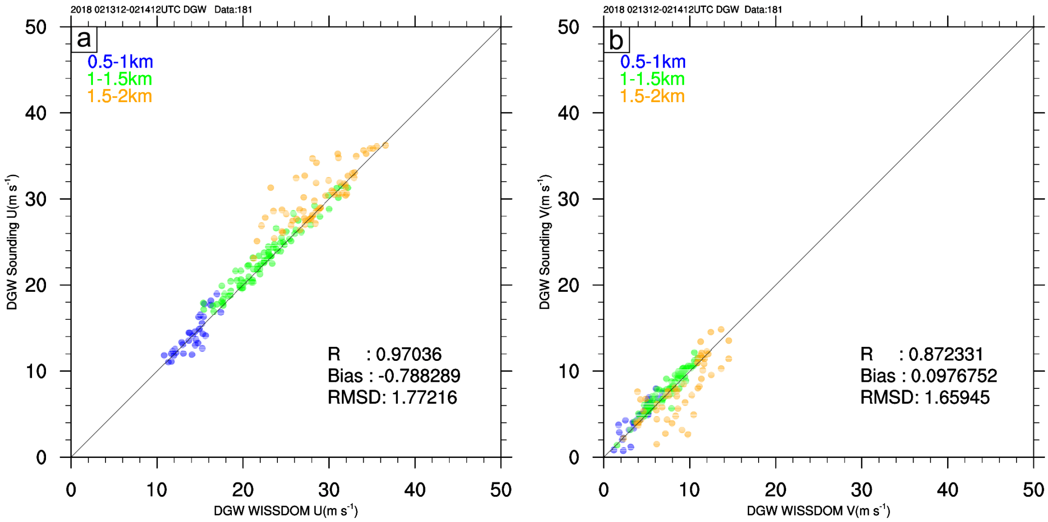

Figure. 6. Scatter plots of (a) u-component winds between the WISSDOM synthesis (x-axis) and sounding observations (y-axis) above the DGW site during the research period. The colors indicate different layers, and the numbers of data points, correlation coefficients, average biases and root mean square deviations are also shown in the figure. (b) The same as (a) but for v-component winds.

Overall, the u-component winds show a high correlation coefficient (exceeding 0.97), low average bias (-0.78 m s^{-1}), and the root mean square deviation (RMSD) of 1.77 m s^{-1}. The correlation coefficient of the v-component is also high (0.87), the average bias is 0.09 m s^{-1}, and the RMSD is 1.65 m s^{-1}.

https://doi.org/10.5194/amt-2022-218
Preprint. Discussion started: 1 August 2022

Atmospheric Measurement Techniques
Discussions

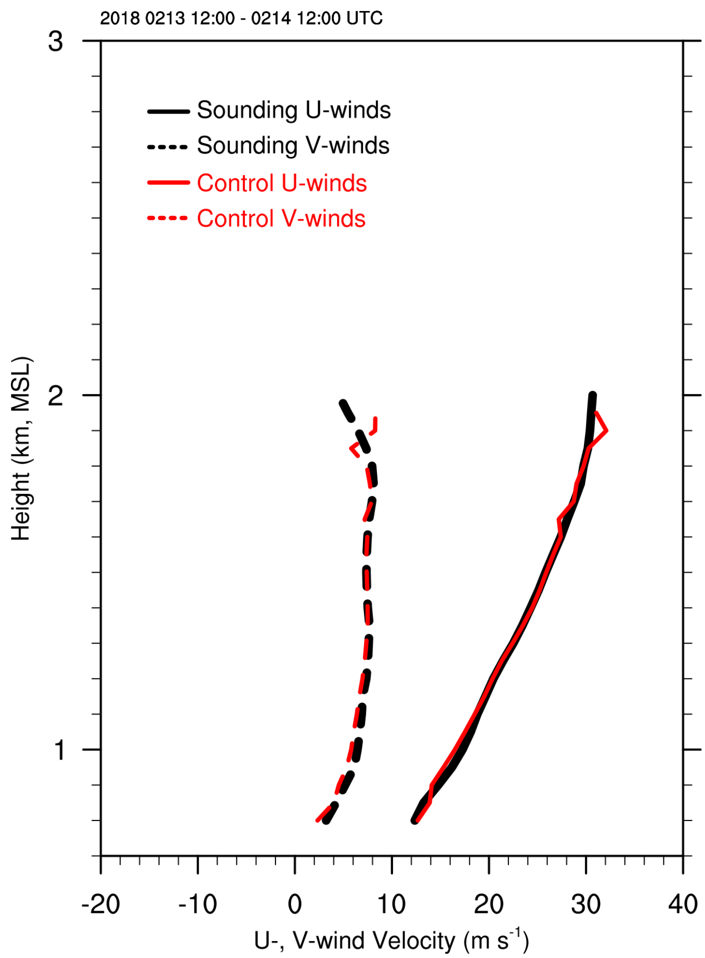

Figure 7. Vertical wind profiles of average horizontal winds derived from the WISSDOM synthesis (red lines and vectors) and sounding observations (black lines and vectors) above the DGW site from 12:00 UTC on 13 to 12:00 UTC on 14 Feb. 2018. Solid lines indicate u-component winds (m s^{-1}), and dashed lines indicate v-component winds (m s^{-1}).

The vertical profiles of the averaged u- and v-component winds for the period of 12:00 UTC on 13 to 12:00 UTC on 14 Feb. 2018 are shown in Fig. 7 for the WISSDOM synthesis (red) and sounding observations (black) launched from the DGW site. The average profiles agree well except for the height above 1.5 km MSL, slight discrepancies of u- and v-component winds (< 1 m s^{-1}). Their statistical errors during the entire research period were quantified by the box plot shown in Fig. 8.

https://doi.org/10.5194/amt-2022-218
Preprint. Discussion started: 1 August 2022

The maximum difference in wind directions between the WISSDOM synthesis and sounding observations is small at all layers. The interquartile range (IQR) and median values of the wind direction are also smaller (between ~0 and 2.5 degrees) except for relatively larger IQR existed (between ~−5 and 5 degrees) and larger median values (between ~0 and 5 degrees) at the lowest level during the entire research period (Fig. 8a). Basically, the IQR and median values of the wind direction are close to 0 degrees above 1 km MSL. Fig. 8b shows the difference in wind speed between the WISSDOM synthesis and sounding observations. The wind speed derived from WISSDOM was slightly underestimated in the layers between ~0.85 and 1.3 km MSL. The median values of the wind speed were between −1 and 0.5 m s^{-1}, and the IQR of wind speed was between −2 and 0.5 m s^{-1}. Above 1.3 km MSL, the differences in wind speed are small as their median values are close to 0 m s^{-1}.

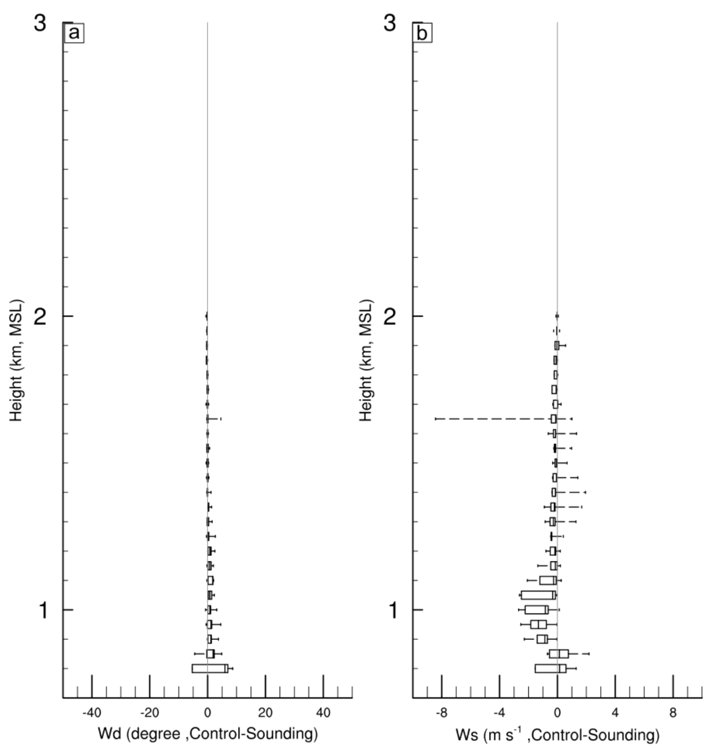

Figure 8. The box plot of average (a) wind direction discrepancies between the WISSDOM synthesis and sounding observations above the DGW site during the research period. (b) Same as (a) but for the wind speed.

https://doi.org/10.5194/amt-2022-218
Preprint. Discussion started: 1 August 2022

Atmospheric Measurement Techniques Discussions

4.2.3 Lidar QVP

The lidar QVP is another observational reference used to evaluate the performance of derived winds from the WISSDOM synthesis. The scatter plots of the horizontal winds derived from WISSDOM and lidar QVP at the DGW site are shown in Fig. 9. The strength of the u-component winds increases with height in the range between approximately 10 m s^{-1} and 40 m s^{-1} from the surface up to ~2.5 km MSL (Fig. 9a). Although the results show a relatively high correlation coefficient (0.84) for the u-component winds from lower to higher layers in the entire research period, the degree of scatter is larger than that in Fig. 6a. The average bias and RMSD of the u-component winds are 2.83 m s^{-1} and 3.69 m s^{-1}, respectively. The correlation coefficient of v-component winds is lower (0.35) in association with low wind speed (<15 m s^{-1}) from the surface to 2.5 km MSL (Fig. 9b). The average bias and RMSD of the v-component winds are 2.26 m s^{-1} and 2.92 m s^{-1}, respectively. The results of these scatter plot analyses are summarized in Table 2. Basically, the u-component winds have high correlations, relatively lower bias, and lower RMSD than the v-component winds because the environmental winds are more westerly.

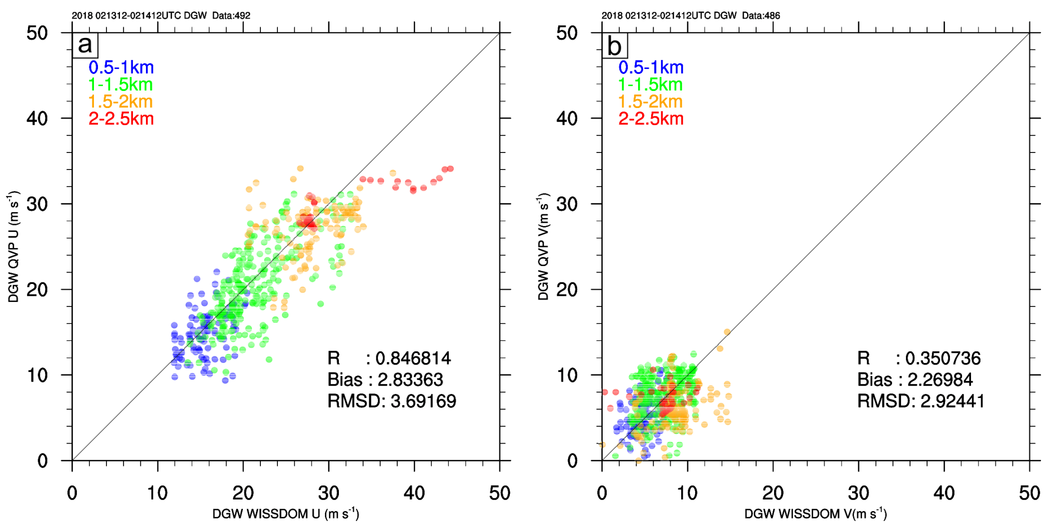

Figure 9. The same as Fig. 6 but for (a) u-component winds between the WISSDOM synthesis (x-axis) and lidar QVP (y-axis). (b) The same as (a) but for v-component winds.

https://doi.org/10.5194/amt-2022-218
Preprint. Discussion started: 1 August 2022

Atmospheric Measurement Techniques
Discussions

Table 2 Summary of the intercomparisons between WISSDOM and observations

		Correlation coefficient	Average bias (m s^{-1})	RMSD (m s^{-1})
WISSDOM-sounding	u-component	0.97	-0.78	1.77
	v-component	0.87	0.09	1.65
WISSDOM-lidar QVP	u-component	0.84	2.83	3.69
	v-component	0.35	2.26	2.92

Compared to the sounding observations, additional w-component winds are available in lidar QVP, which allows us to check their discrepancies in 3D winds. However, most of the vertical velocity observations were quite weak (approximately ±0.2 m s^{-1}) above the DGW site, and relatively low reliability of the derived vertical velocity could be expected in this event. Therefore, the average vertical profiles of 3D winds were utilized to qualitatively check the discrepancies between WISSDOM synthesis and lidar QVP during the research period (Fig. 10). The results show that the average u-component winds have relatively smaller discrepancies (approximately <1 m s^{-1}) between the WISSDOM synthesis (marked as WISS-U in Fig. 10) and lidar QVP (marked as QVP-U) below ~1.3 km MSL at the DGW site. In contrast, there were larger discrepancies (approximately >2 m s^{-1}) between 1.3 km and 2 km MSL. The average v-component winds derived from WISSDOM (marked as WISS-V) and lidar QVP (QVP-V) were generally weak, and the ranges of WISS-V and QVP-V were between ~2 m s^{-1} and 8 m s^{-1}. Generally, the vertical profiles of WISS-V were nearly overlain with QVP-V, and their discrepancies existed in the height range 1.6~2.0 km MSL (maximum ~4 m s^{-1}). Smaller (larger) discrepancies of w-component winds were significantly below (above) the height at ~1.3 km MSL (maximum discrepancies ~0.6 m s^{-1} at 1.7 km MSL). Despite the larger discrepancies, the similar patterns of W can also be shown. In summary, the discrepancies in the 3D winds between the WISSDOM synthesis and lidar QVP were small in the lower layers and large in the higher layers because the observational data from lidars and AWSs provided good quality and sufficient wind information at the lower layers but not in the higher layers (lower coverages of lidar data above 1.3 km MSL, cf. Fig. 4).

https://doi.org/10.5194/amt-2022-218
Preprint. Discussion started: 1 August 2022

Atmospheric Measurement Techniques Discussions

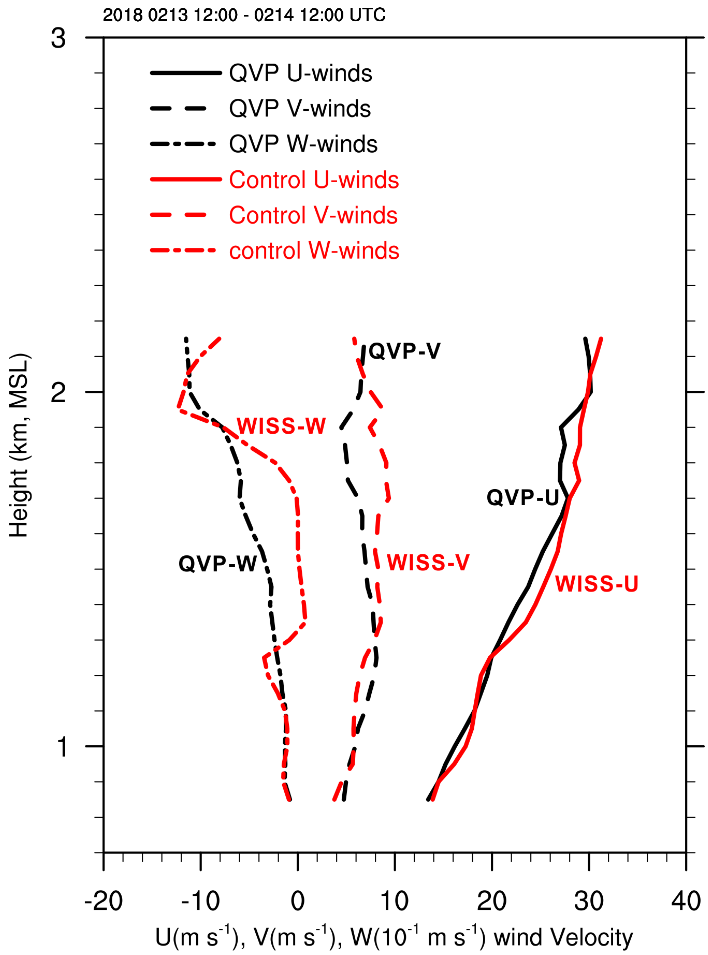

Figure 10. Vertical wind profiles of average 3D winds derived from the WISSDOM synthesis (red lines and vectors) and lidar QVP (black lines and vectors) above the DGW site from 12:00 UTC on 13 to 12:00 UTC on 14 Feb. 2018. Solid lines indicate u-component winds (m s^{-1}), dashed lines indicate v-component winds (m s^{-1}), and dash-dotted lines indicate w-component winds (1×10^{1} m s^{-1}). The u-, v-, and w-component winds derived from the WISSDOM synthesis (lidar QVP) were marked by WISS-U (QVP-U), WISS-V (QVP-V), and WISS-W (QVP-W), respectively.

Fig. 11 shows the quantile distribution of statistical errors of wind direction, wind speed and vertical velocity between the WISSDOM synthesis and lidar QVP during the research period. The IQR of the wind direction is smaller (−5~5 degrees) in the layers from 0.85 km to 1.5 km MSL and turns to approximately −10~0 degrees above 1.5 km MSL. The median values of wind direction are smaller −5~5 degrees) from near the surface to the upper layers (Fig. 11a). Fig. 11b

https://doi.org/10.5194/amt-2022-218
Preprint. Discussion started: 1 August 2022

Atmospheric Measurement Techniques Discussions

shows that the median values (IQR) of wind speed are approximately −1~1 m s^{-1} (−2~2 m s^{-1}) below 1.5 km MSL, and they all become larger with heights above 1.5 km MSL (between −1 and 3 m s^{-1} for median values and −4~4 m s^{-1} for the IQR). The statistical error of the vertical velocity reveals that the IQR is −0.2~0.2 m s^{-1} (−0.8~0.8 m s^{-1}) below (above) 1.3 km MSL, and the median values are 0~0.2 m s^{-1} −0.2~0.6 m s^{-1}) below (above) 1.3 km MSL. The results of statistical errors are summarized in Table 3.

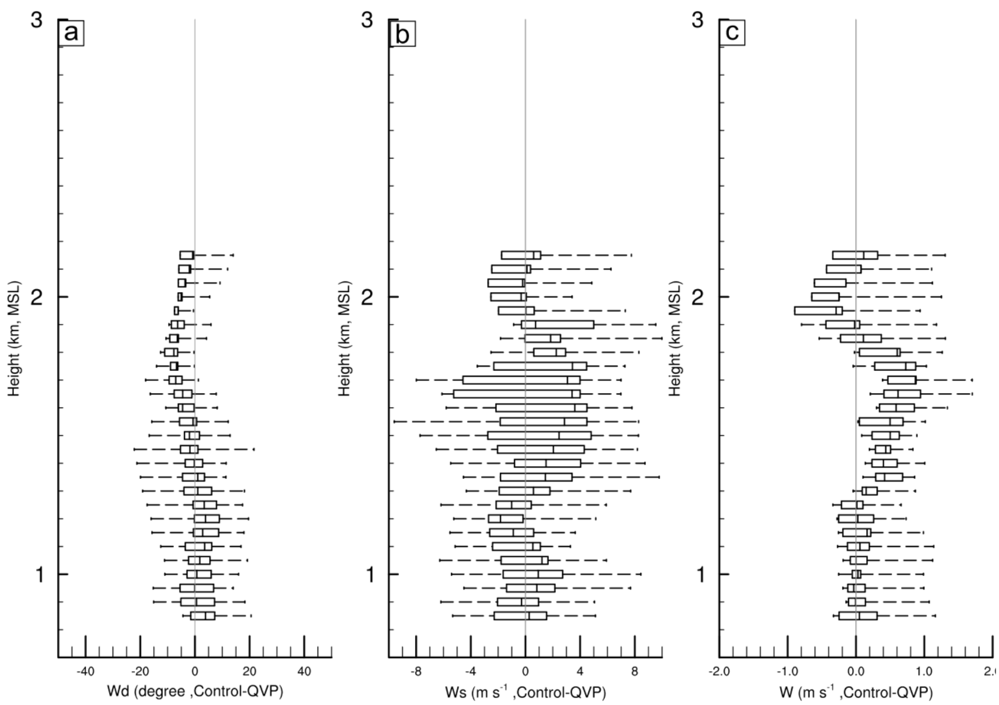

Figure 11. The box plot of average (a) wind direction discrepancies between the WISSDOM synthesis and sounding observations above the DGW site during the research period. (b) Same as (a) but for the wind speed. (c) Same as (a) but for the w-component winds.

https://doi.org/10.5194/amt-2022-218
Preprint. Discussion started: 1 August 2022

Table 3 Summary of the statistical errors between WISSDOM and observations

		Interquartile range (IQR)	Median values
WISSDOM-sounding	wind direction	0~2.5 (deg.)	0~2.5 (deg.)
	wind speed	−2~0.5 (m s^{-1})	−1~0.5 (m s^{-1})
WISSDOM-lidar QVP	wind direction	−10~5 (deg.)	−5~5 (deg.)
	wind speed	-4~4 (m s^{-1})	−1~3 (m s^{-1})
	w-component winds	−0.8~0.8 (m s^{-1})	−0.2~0.6 (m s^{-1})

5. Sensitivity test with various datasets, data implementation and weighting coefficients

5.1 Impacts of various datasets (Experiment A)

In this session, the impacts of various datasets implemented in the WISSDOM synthesis were evaluated. The basic setting of Experiment A is the same as that of the WISSDOM control run (cf. Table 1) except for four designs in Experiment A. The details of these four designs are summarized in Table 4 as the control run without the lidar observations (A-1), the control run without the AWS observations (A-2), the control run without the sounding observations (A-3) and the control run without the LDAPS data (A-4). The discrepancies of 3D winds were examined between the control run and each design in Experiment A. Since the environmental wind speed is nearly comprised of uniform westerlies in this event, the results only show the difference in u-component winds between control run and each design (A-1~A-4) in Fig. 12.

Fig. 12a reveals the discrepancies in horizontal u-component winds at 800 m MSL as the A-1 is subtracted from the control run. This result reflects the impacts of lidar observations on the u-component winds in the WISSDOM synthesis. The most significant contributions from the lidar observations are the high wind speed existing near the DGW site in a relatively narrow

https://doi.org/10.5194/amt-2022-218
Preprint. Discussion started: 1 August 2022

valley. The mechanisms of the accelerated wind speed due to the channeling effect in this local area were verified by our previous study (Tsai et al. 2022). The lidar observations also contributed to the high wind speed in another area near the western side of the MHS site (128.68°E, 37.66°N). Based on the analysis in the vertical cross section of u-component winds in A-1 (Fig. 12b), the lidar observations significantly affected the high wind speed only in the lower levels (below ~900 m MSL) but not in the higher levels. Lidar observations provided sufficient coverage only for lower levels and not higher levels (cf. Fig. 4).

Table 4 Experiment setting (sensitivity testing)

Control run	Various datasets	Including Doppler lidars, AWSs, Soundings, LDAPS
	Interpolation of AWS	RI: 1.0 km, VE: 90%
	Weighting Coefficient	AWS (α_7): 10^6 Doppler Lidars (α_1): 10^6 LDAPS (α_8): 10^3
Experiment A	Various datasets	A-1 Excluding Doppler Lidars A-2 Excluding AWSs A-3 Excluding Soundings A-4 Excluding LDAPS
Experiment B	Interpolation of AWS	B-1 RI: 0.5 km, VE: 50% B-2 RI: 0.5 km, VE: 90% B-3 RI: 1.0 km, VE: 50% B-4 RI: 2.0 km, VE: 50% B-5 RI: 2.0 km, VE: 90%
Experiment C	Weighting Coefficient (constraints)	C-1 AWS (α_7): 10^3 C-2 Doppler Lidars (α_1): 10^3 C-3 LDAPS (α_8): 10^6

The AWSs have negative impacts on the u-component winds in most areas at 800 m MSL in A-2 (Fig. 12c), especially in the western areas of the MHS site. Negative contributions of the u-component winds produced by the AWS observations were restricted near the surface, and the low wind speed area was extended to ~100 m above the surface (Fig. 12d). The contributions of

https://doi.org/10.5194/amt-2022-218
Preprint. Discussion started: 1 August 2022

the u-component winds from the sounding observations were weak near the DGW sounding site in A-3 (Figs. 12e and 12f). The impacts of u-component winds from the LDAPS datasets were rather smaller in most of analysis area. in A-4 (Figs. 12g and 12h).

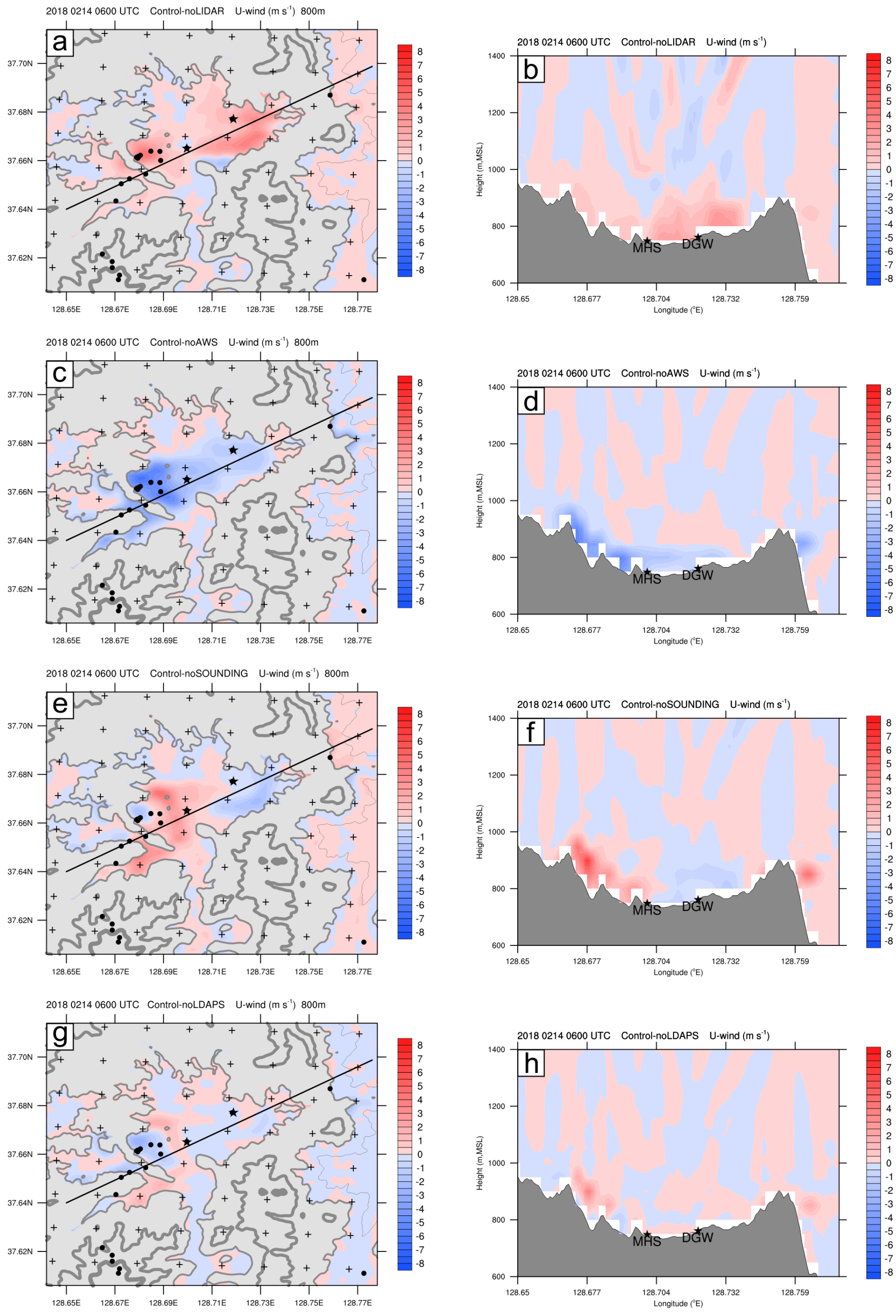

https://doi.org/10.5194/amt-2022-218
Preprint. Discussion started: 1 August 2022

Atmospheric Measurement Techniques Discussions

Figure 12. (a) The discrepancies in horizontal u-component winds between the control run and A-1 at 800 m MSL at 06:00 UTC on 14 Feb. 2018. (b) The same as (a) but for the vertical section along the black line in (a). (c) and (d) are the same as (a) and (b) but for A-2. (e) and (f) are the same as (a) and (b) but for A-3. (g) and (h) are the same as (a) and (b) but for A-4.

Averaged discrepancies of derived 3D winds for each vertical level are shown in Fig. 13. These results summarized a series of sensitivity tests if the WISSDOM synthesis lacks certain data inputs (i.e., A-1~A-4 in Experiment A) for derived u-, v- and w-component winds in the test domain. Overall, the maximum absolute value of averaged discrepancies for Experiment A are smaller than approximately 0.5 m s^{-1}, which are the discrepancies of the u-component winds for A-1 and A-2 located at 800 m MSL. Except for these values, the values of the derived u-, v- and w-component winds for A-1~A-2 are approximately smaller than 0.2 m s^{-1} from the surface up to the top in the test domain.

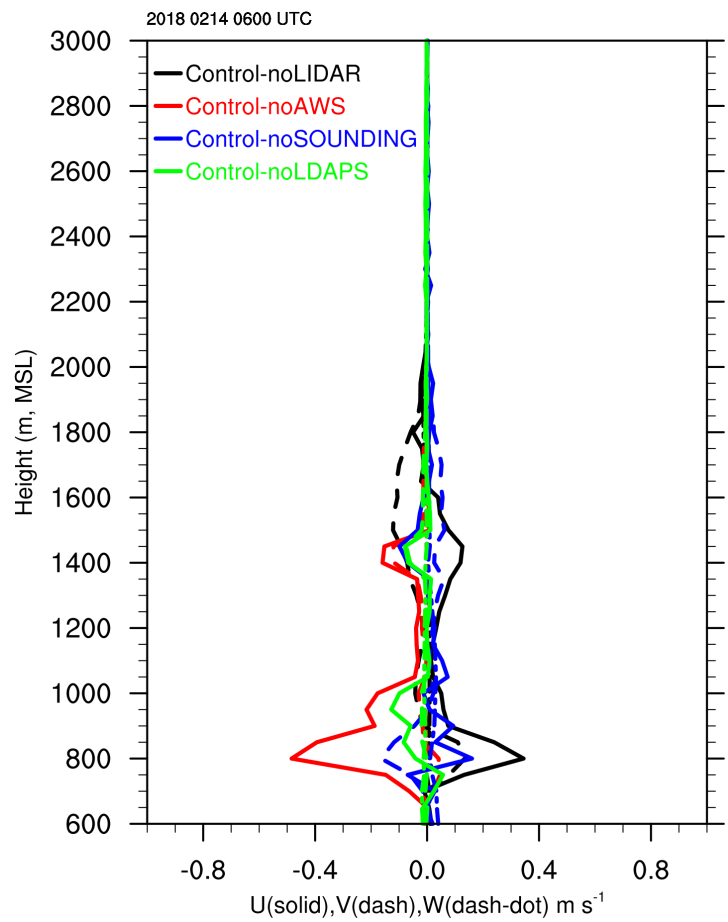

Figure 13. Vertical profiles of averaged discrepancies of 3D winds for each design in Experiment A at 06:00 UTC on 14 Feb. 2018. The averaged discrepancies of u-, v- and w-component winds were plotted by solid, dash, and dash-dot lines, and the black, red, blue and green lines indicate A-1, A-2, A-3 and A-4, respectively.

5.2 Radius of influence (RI) and vertical extension for the AWS (Experiment B)

Experiment B was performed to check the discrepancies in 3D winds between the control run and the different settings of RI and VE with the AWS observations. There were five designs (B-1~B-5) in Experiment B with the ranges of RI (VE) between 0.5 km (50%) and 2 km (90%). The details are shown in Table 4. The horizontal u-component winds at 800 m MSL and the vertical structure of Experiment B at one time step (06:00 UTC on 14 February 2018) are shown in Fig. 14. An unusual circular area with positive discrepancies around the MHS site was depicted in B-

https://doi.org/10.5194/amt-2022-218
Preprint. Discussion started: 1 August 2022

1 (Figs, 14a and 14b), which may have been produced by the insufficient RI distance and VE. Relatively smaller RI and VE values can only include relatively less wind information if the distances between ~~AWS stations~~ are large. Enlarging the RI and VE are required to appropriately include more wind information from the AWS observations. Figs. 14c and 14d show the results of B-2 as VE reached 90%. Although the unusual circle vanished, there were discontinuities with negative values near the northern and southern areas of the MHS site and positive areas surrounding the AWSs (128.68°E, 37.66°N). The setting of B-3 was similar to that of the control run except that the VE was 50%. The discrepancies were relatively small, albeit dense AWS stations contributed even smaller negative values in the western areas of the MHS sites (Figs. 14g and 14h). Obviously, positive discrepancies appeared near the northern and southern areas of the MHS site in B-4 and B-5 (Figs. 14g-j). The impacts of the AWS with various settings (B-1~B-5) on the discrepancies in u-component winds were both restricted near the surface, even with a larger RI and high VE.

https://doi.org/10.5194/amt-2022-218
Preprint. Discussion started: 1 August 2022

Atmospheric Measurement Techniques Discussions

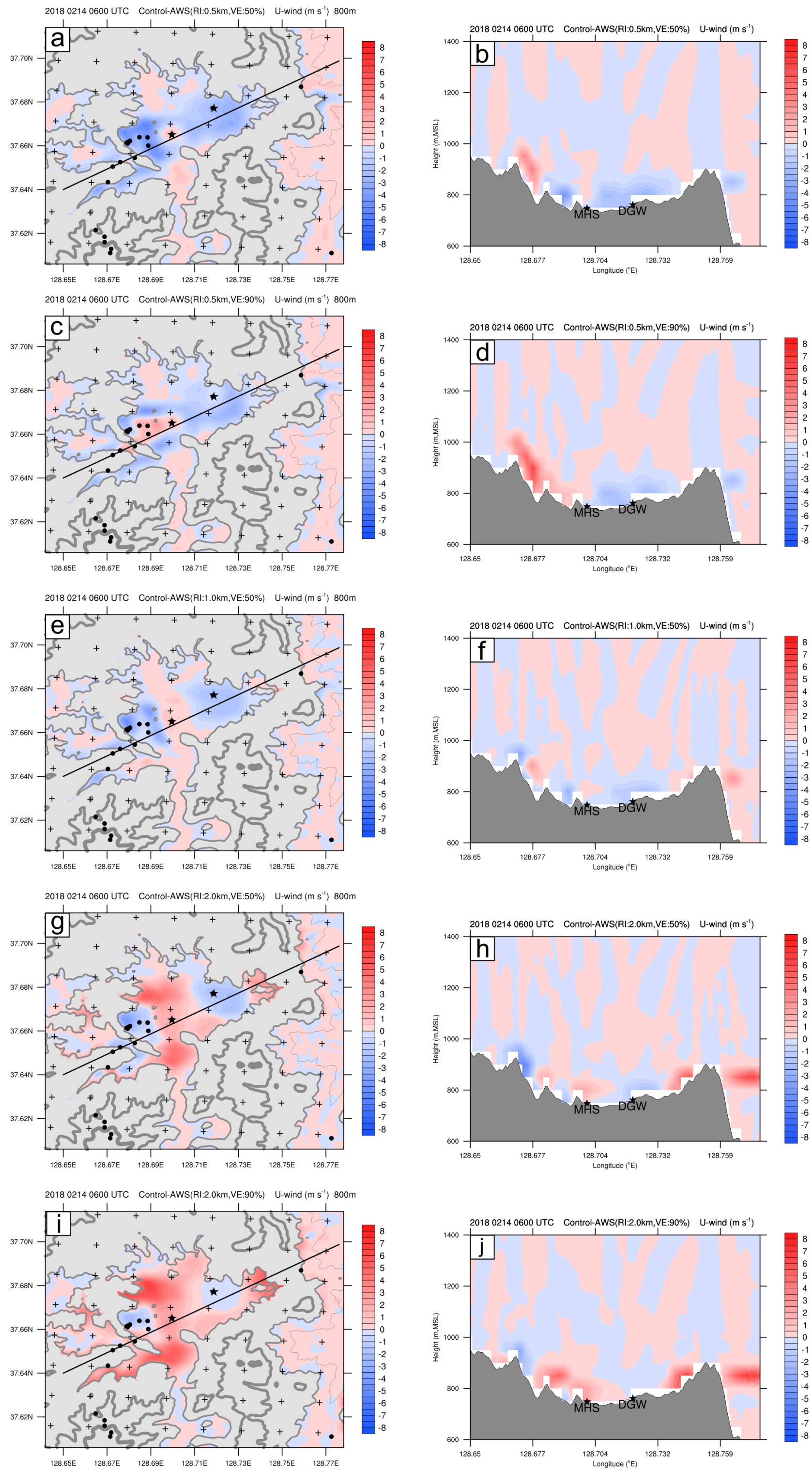

616

https://doi.org/10.5194/amt-2022-218
Preprint. Discussion started: 1 August 2022

Figure 14. The same as Fig.12, but (a) and (b) for B-1. (c) and (d) are the same as (a) and (b) but for B-2. (e) and (f) are the same as (a) and (b) but for B-3. (g) and (h) are the same as (a) and (b) but for B-4. (i) and (j) are the same as (a) and (b) but for B-5.

Fig. 15 shows the vertical profiles of averaged discrepancies of derived 3D winds in Experiment B. This figure summarizes the results of sensitivity testing with different settings of the RI and VE in WISSDOM (i.e., B-1~B-5 in Experiment B, shown in Table 4) for derived u-, v- and w-component winds in the test domain. The maximum discrepancies of u-component winds in B-1, B-2 and B-3 were quite small at only 0.4, 0.3 and 0.2 m s^{-1}, respectively. Nevertheless, the maximum discrepancies of u-component winds for B-4 and B-5 were larger than 0.6 m s^{-1} and even exceeded ~1 m s^{-1}. Although the discrepancies in the u-component winds in B-1 were small, the discrepancies in the v-component winds in B-1 reveal unusual patterns, with larger positive values at ~1100 m MSL and negative values at ~1800 m MSL (black dashed line in Fig. 15), the possible reason is the minimizations of cost function are not converged well because relatively few and weak v-component winds were included in B-1. Except for this value, the maximum discrepancies of v-component winds were small for B-2~B-5, and the maximum discrepancies of w-component winds were also small for all of Experiment B. Note that B-3 always has the smallest discrepancies with the derived 3D winds because the setting is quite similar to the control run.

https://doi.org/10.5194/amt-2022-218
Preprint. Discussion started: 1 August 2022

Atmospheric Measurement Techniques Discussions

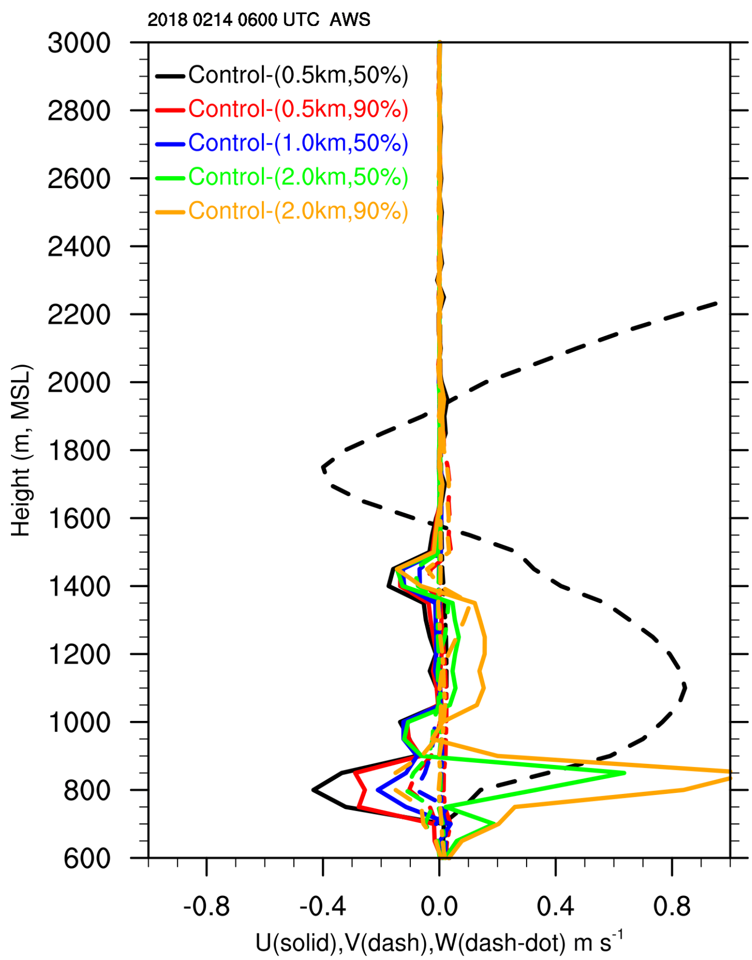

Figure 15. The same as Fig. 13. but for B-1~B-5.

5.3 Different weighting coefficients for the constraints (Experiment C)

Experiment C was designed to check the discrepancies in the derived u-component winds between the control run and experimental runs with different weighting coefficients for each constraint related to the AWS, lidar and LDAPS (corresponding to C-1, C-2 and C-3 in Table 4). Originally, the weighting coefficients for the AWS and lidar observations were set to 10^6, and the value was 10^3 for the LDAPS dataset (i.e., control run, Table 1). The results of Experiment C show significant negative discrepancies in u-component winds near the surface in C-1, especially

https://doi.org/10.5194/amt-2022-218
Preprint. Discussion started: 1 August 2022

Atmospheric Measurement Techniques Discussions

in the areas next to the AWSs (128.68°E, 37.66°N). The discrepancies for C-1 (Figs. 16a and 16b) and C-2 (Figs. 16c and 16d) are similar to those for A-2 (Figs. 12c and 12d) and A-1 (Figs. 12a and 12b), respectively. The inputs of AWSs and lidar both contributed relatively weak impacts to the WISSDOM synthesis when the weighting coefficient was set to 10^3. Irrational patterns were depicted when the weighting coefficient of LDAPS inputs increased to 10^6, and larger and positive discrepancies were crowded into most areas in the valley (i.e., C-3, Figs. 16e). Larger and positive discrepancies existed only near the surface, and there were negative discrepancies between approximately 1000 m and 1400 m (Fig. 16f). Note that the influences of sounding observations also existed above the DGW site in scenario C-3.

The vertical profiles of averaged discrepancies of derived 3D winds in Experiment C are shown in Fig. 17. Absolute values of the discrepancies in the u-, v- and w-component winds are smaller than 1 m s^{-1}, except for the discrepancies in the v-component winds with low weighting of the AWS observations (i.e., C-1) and the discrepancies in the u- and v-component winds with the high weighted LDAPS (i.e., C-3). The discrepancies in the v-component winds in C-1 exceeded −5 m s^{-1} at ~1100 m MSL and were larger than −15 m s^{-1} above 2600 m MSL. These unreasonable characteristics are also shown as the discrepancies in the v-component winds in B-1 (cf. Fig. 15). The discrepancies in the u- and v-component winds in C-3 are 15 m s^{-1} and 4 m s^{-1}, respectively, in the layers between 700 and 900 m MSL. Alternative positive and negative discrepancies in the range of -3 to 3 m s^{-1} for the u-component winds in C-3 were found above 1000 m MSL.

https://doi.org/10.5194/amt-2022-218
Preprint. Discussion started: 1 August 2022

Atmospheric Measurement Techniques Discussions

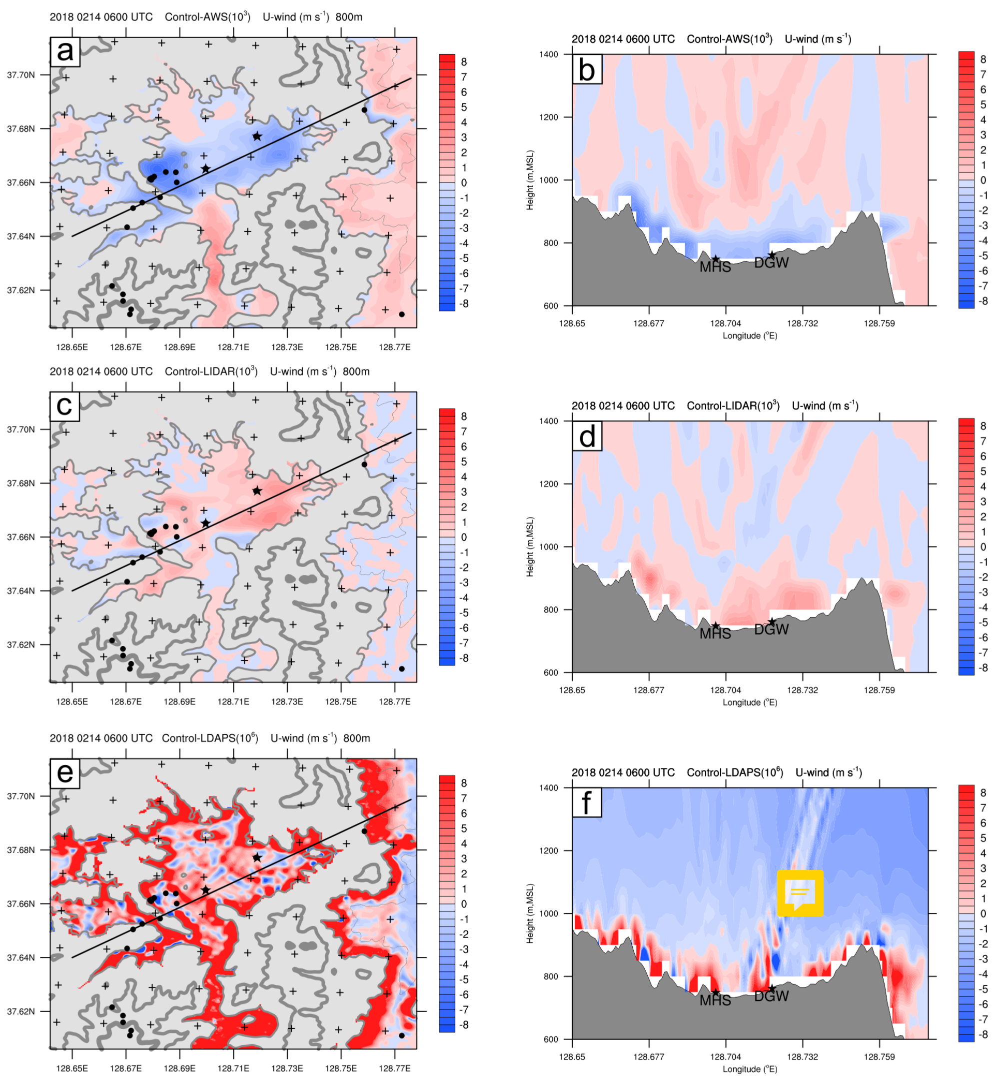

Figure 16. The same as Fig.12, but (a) and (b) for C-1. (c) and (d) are the same as (a) and (b) but for C-2. (e) and (f) are the same as (a) and (b) but for C-3.

https://doi.org/10.5194/amt-2022-218
Preprint. Discussion started: 1 August 2022

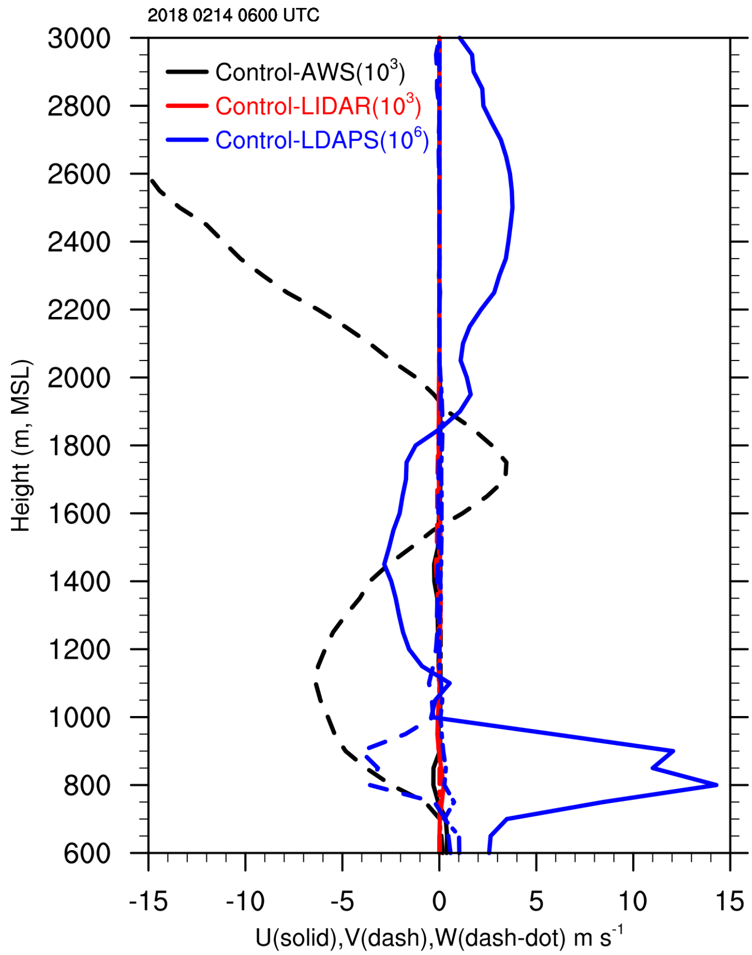

Figure 17. The same as Fig. 13 but for C-1~C-3.

6. Conclusion

A modified WISSDOM synthesis scheme was developed to derive high-quality 3D winds under clear-air conditions. The main difference from the original version is that multiple lidar observations were used, and high-resolution 3D winds (50 m horizontally and vertically) were first derived in the newly developed WISSDOM scheme. In addition, all available datasets were included as one of the constraints in the cost function in this study. The data implementation and the detailed principles of the newly developed WISSDOM were also elaborated. This newly developed WISSDOM scheme was performed over the TMR to retrieve 3D winds during a strong wind event during ICE-POP 2018. The performance was evaluated via a series of sensitivity tests and compared with conventional observations.

The intercomparisons of horizontal winds during the entire research period reveal a relatively high correlation coefficient between the WISSDOM synthesis and sounding's u- (v-) component winds exceeding 0.97 (0.87) at the DGW site. Furthermore, the average bias is −0.78 m s^{-1} (0.09 m s^{-1}), and the RMSD is 1.72 m s^{-1} (1.65 m s^{-1}) for the u- (v-) component winds. The intercomparisons of 3D winds between the WISSDOM synthesis and lidar QVP also showed a higher correlation coefficient (0.84) for u-component winds, but a relatively smaller correlation coefficient remained at 0.35 for v-component winds in this strong wind event. The average bias (RMSD) of u-component winds is 2.83 m s^{-1} (3.69 m s^{-1}), and the average bias and RMSD of v-component winds are 2.26 m s^{-1} and 2.92 m s^{-1}, respectively (cf. Table 2). Chen (2019) analyzed the correlations between 3D winds derived from radar and observations in several typhoon cases; the mean correlation coefficient ranged from 0.56 to 0.86, and the RMSD was between 1.13 and 1.74 m s^{-1}. Compared to their results, only u-component winds have relatively higher correlation coefficients, but the RMSD values are slightly higher in this study, which may have been caused by the high variability in westerly winds associated with the moving LPS. The statistical error results of the winds between the WISSDOM synthesis and observations show a good performance of the retrieved 3D winds in this strong wind event (Table 3). Generally, the median values of wind directions are within 5 degrees. Compared with lidar QVP (sounding observations) the median values of the wind speed are approximately −1~3 m s^{-1} (−1~0.5 m s^{-1}) and the vertical velocity is within −0.2~0.6 m s^{-1}. Compared with lidar QVP (sounding observations) above the DGW site, the interquartile range of wind directions is −10~5 (0-2.5) degrees, the wind speed is approximately -4~4 m s^{-1} (−3~1 m s^{-1}) and the vertical velocity is −0.8~0.8 m s^{-1}.

A control run (see the basic setting in Table 1) was set to explore the importance of acquired

https://doi.org/10.5194/amt-2022-218
Preprint. Discussion started: 1 August 2022

observation datasets, various distances of RI, VE from the AWS observations, and the weighting coefficient for each constraint (i.e., Experiments A-C, Table 4). The results of Experiment A show that the lidar and AWS play critical roles in the derived horizontal winds, and the lidars (AWSs) provided positive (negative) contributions in stronger (weaker) wind speeds near the surface. The sounding and the LDAPS provided relatively smaller impacts on the derived horizontal winds from the WISSDOM synthesis. In Experiment B, the smallest discrepancies in 3D winds were depicted when the RI (VE) was set to 1 km (50%). However, there were larger discrepancies in 3D winds (from −0.4 m s^{-1} to ~1 m s^{-1}) when the RI was set at 0.5 km and 2 km, and the VE was set between 50% and 90% (cf. Fig. 15). In Experiment C, significant discrepancies in 3D winds appeared by decreasing (raising) the weighting coefficient from the AWS observations (LDPAS datasets).

This study demonstrated that reasonable patterns of 3D winds were derived by the newly developed WISSDOM synthesis scheme in a strong wind event. In the future, many cases are required to check the performance of this newly developed WISSDOM scheme with different synoptic weather systems under clear-air conditions in different seasons. In addition, knowing the detailed kinematic fields will help us to identify where the flow accelerates/decelerates over complex terrain. Thus, the possible mechanisms of extremely strong winds in South Korea will be well documented through combinations with derived dynamic fields (Tsai et al., 2018, 2022), thermodynamic fields (Liou et al., 2019), observations and simulations. Furthermore, the new version of WISSDOM has broad applications in site surveys of wind turbines, wind energy, monitoring wildfires, outdoor sports in mountain ranges and aviation security.

https://doi.org/10.5194/amt-2022-218
Preprint. Discussion started: 1 August 2022

Atmospheric Measurement Techniques
Discussions

Code and data availability. The scanning Doppler lidars, AWS, sounding and wind profiler data used in this study are available through zenodo: https://doi.org/10.5281/zenodo.6537508. The LDAPS dataset is freely available from the KMA website (https://data.kma.go.kr).

Acknowledgments. This work was supported by the National Research Foundation of Korea (NRF) grant funded by the Korea government (MSIT) (No. 2021R1A4A1032646) and by the Korea Meteorological Administration Research and Development Program under Grant KMI2022-00310.

Author contributions. This work was made possible by contribution from all authors. Conceptualization, CLT, GWL; methodology, CLT, YCL, and KK; software, CLT, YCL, and KK; validation, KK, YCL, and GWL; formal analysis, CLT, and KK; investigation, CLT, and GWL; writing—original draft preparation, CLT; writing—review and editing, GWL, YCL and KK; visualization, CLT; supervision, GWL; funding acquisition, GWL. All authors have read and agreed to the published version of the manuscript.

Competing interests. The authors declare that they have no conflict of interest.

Special issue statement. This article is part of the special issue "Winter weather research in complex terrain during ICE-POP 2018 (International Collaborative Experiments for Pyeongchang 2018 Olympic and Paralympic winter games) (ACP/AMT/GMD inter-journal SI)". It is not associated with a conference.

https://doi.org/10.5194/amt-2022-218
Preprint. Discussion started: 1 August 2022

References

Bell, M. M., Montgomery, M. T., and Emanuel, K. A.: Air–sea enthalpy and momentum exchange at major hurricane wind speeds observed during CBLAST, *J. Atmos. Sci.*, **69**, 3197–3222, https://doi.org/10.1175/JAS-D-11-0276.1, 2012.

Bell, T. M., Klein, P., Wildmann, N., and Menke, R.: Analysis of flow in complex terrain using multi-Doppler lidar retrievals, *Atmos. Meas. Tech.*, **13**, 1357–1371, https://doi.org/10.5194/amt-13-1357-2020, 2020.

Chen, Y.-A.: Verification of multiple-Doppler-radar derived vertical velocity using profiler data and high resolution examination over complex terrain, M.S. thesis, National Central University, 91 pp., 2019.

Choi, D., Hwang, Y., Lee, YH.: Observing Sensitivity Experiment Based on Convective Scale Model for Upper-air Observation Data on GISANG 1 (KMA Research Vessel) in Summer 2018. *Atmosphere*, **30**, 17–30, 2020 (Korean with English abstract).

Cha, T.-Y. and Bell, M. M.: Comparison of single-Doppler and multiple-Doppler wind retrievals in Hurricane Matthew (2016), *Atmos. Meas. Tech.*, **14**, 3523–3539, https://doi.org/10.5194/amt-14-3523-2021, 2021.

Choukulkar, A., Brewer, W. A., Sandberg, S. P., Weickmann, A., Bonin, T. A., Hardesty, R. M., Lundquist, J. K., Delgado, R., Iungo, G. V., Ashton, R., Debnath, M., Bianco, L., Wilczak, J. M., Oncley, S., and Wolfe, D.: Evaluation of single and multiple Doppler lidar techniques to measure complex flow during the XPIA field campaign, *Atmos. Meas. Tech.*, **10**, 247–264, https://doi.org/10.5194/amt-10-247-2017, 2017.

Colle, B. A., and Mass, C. F.: High-Resolution Observations and Numerical Simulations of Easterly Gap Flow through the Strait of Juan de Fuca on 9–10 December 1995. *Mon. Wea. Rev.*, **128**, 2398–2422,

Cressman, G. P.: An operational objective analysis system. *Mon. Wea. Rev.*, **87**, 367–374, 1959.

https://doi.org/10.5194/amt-2022-218
Preprint. Discussion started: 1 August 2022

Hill, M., R. Calhoun, H. J. S. F., Wieser, A., Dornbrack, A., Weissmann, M., Mayr, G., and Newsom, R.: Coplanar Doppler lidar retrieval of rotors from T-REX, *J. Atmos. Sci.*, **67**, 713–729, 2010.

Jou, B. J.-D., Lee, W.-C., Liu, S.-P., and Kao, Y.-C.: Generalized VTD retrieval of atmospheric vortex kinematic structure. Part I: Formulation and error analysis, *Mon. Weather Rev.*, **136**, 995–1012, https://doi.org/10.1175/2007MWR2116.1, 2008.

Kim D.-J., Kang G., Kim D.-Y., Kim J.-J.: Characteristics of LDAPS-Predicted Surface Wind Speed and Temperature at Automated Weather Stations with Different Surrounding Land Cover and Topography in Korea. *Atmosphere*, **11**, 1224. https://doi.org/10.3390/atmos11111224, 2020.

Kim, J.-H., R. D. Sharman, R. D., Benjamin, S., Brown, J., Park, S.-H. and Klemp, J.: Improvement of Mountain Wave Turbulence Forecast in the NOAA's Rapid Refresh (RAP) Model with Hybrid Vertical Coordinate System, *Weather Forecast*, **34(6)**, 773-780, https://doi.org/10.1175/WAF-D-18-0187.1, 2019

Lee, J., Seo, J., Baik, J., Park, S., and Han, B.: A Numerical Study of Windstorms in the Lee of the Taebaek Mountains, South Korea: Characteristics and Generation Mechanisms. *Atmosphere*, **11**, 431. https://doi.org/10.3390/atmos11040431, 2020.

Lee, J.- T., Ko, K.- Y., Lee, D.- I., You, C.- H., and Liou, Y.- C.: Enhancement of orographic precipitation in Jeju Island during the passage of Typhoon Khanun (2012), *Atmos. Res.*, **201**, 1245–1254. https://doi.org/10.1016/j.atmosres.2017.10.013, 2017.

Lee, W.-C., Marks, F. D., and Carbone, R. E.: Velocity track display – A technique to extract real-time tropical cyclone circulations using a single airborne Doppler radar, *J. Atmos. Ocean. Tech.*, **11**, 337–356, https://doi.org/10.1175/1520-0426(1994)011<0337:VTDTTE>2.0.CO;2, 1994

Lee, W.-C., Jou, B. J.-D., Chang, P.-L., and Deng, S.- M.: Tropical cyclone kinematic structure derived from single-Doppler radar observations. Part I: Interpretation of Doppler velocity

https://doi.org/10.5194/amt-2022-218
Preprint. Discussion started: 1 August 2022

Atmospheric Measurement Techniques Discussions

patterns and the GBVTD technique, *Mon. Weather Rev.*, **127**, 2419–2439, https://doi.org/10.1175/1520-0493(1999)127<2419:TCKSRF>2.0.CO;2, 1999.

Liou, Y.-C., Wang, T.-C. C., Lee, W.-C., and Chang, Y.-J.: The retrieval of asymmetric tropical cyclone structures using Doppler radar simulations and observations with the extended GBVTD technique, *Mon. Weather Rev.*, **134**, 1140–1160, https://doi.org/10.1175/MWR3107.1, 2006.

Liou, Y., and Chang, Y.: A Variational Multiple–Doppler Radar Three-Dimensional Wind Synthesis Method and Its Impacts on Thermodynamic Retrieval. *Mon. Wea. Rev.*, **137**, 3992–4010, https://doi.org/10.1175/2009MWR2980.1, 2009.

Liou, Y., Chang, S., and Sun, J.: An Application of the Immersed Boundary Method for Recovering the Three-Dimensional Wind Fields over Complex Terrain Using Multiple-Doppler Radar Data. *Mon. Wea. Rev.*, **140**, 1603–1619, https://doi.org/10.1175/MWR-D-11-00151.1, 2012.

Liou, Y., Chen Wang, T., Tsai, Y., Tang, Y., Lin, P., and Lee, Y.: Structure of precipitating systems over Taiwan's complex terrain during Typhoon Morakot (2009) as revealed by weather radar and rain gauge observations, *J. Hydrology*, **506**, 14-25. https://doi.org/10.1016/j.jhydrol.2012.09.004, 2013.

Liou, Y., Chiou, J., Chen, W., and Yu, H.: Improving the Model Convective Storm Quantitative Precipitation Nowcasting by Assimilating State Variables Retrieved from Multiple-Doppler Radar Observations. *Mon. Wea. Rev.*, **142**, 4017–4035, https://doi.org/10.1175/MWR-D-13-00315.1, 2014.

Liou, Y., Chen Wang, T., and Huang, P.: The Inland Eyewall Reintensification of Typhoon Fanapi (2010) Documented from an Observational Perspective Using Multiple-Doppler Radar and Surface Measurements. *Mon. Wea. Rev.*, **144**, 241–261, https://doi.org/10.1175/MWR-D-15-0136.1, 2016.

Mass, C. F., and Ovens, D.: The Northern California Wildfires of 8–9 October 2017: The Role

https://doi.org/10.5194/amt-2022-218
Preprint. Discussion started: 1 August 2022

of a Major Downslope Wind Event. *Bull. Amer. Meteor. Soc.*, **100**, 235–256, https://doi.org/10.1175/BAMS-D-18-0037.1, 2019.

Mohr, C. G., and Miller, L. J. : CEDRIC—A software package for Cartesian Space Editing, Synthesis, and Display of Radar Fields under Interactive Control. Preprints, *21st Conf. on Radar Meteorology*, Edmonton, AB, Canada, Amer. Meteor. Soc., 569–574, 1983.

Oue, M., Kollias, P., Shapiro, A., Tatarevic, A., and Matsui, T.: Investigation of observational error sources in multi-Doppler-radar three-dimensional variational vertical air motion retrievals, *Atmos. Meas. Tech.*, **12**, 1999–2018, https://doi.org/10.5194/amt-12-1999-2019, 2019.

Park, J.-R., Kim, J.-H., Shin, Y., Kim, S.-H., Chun, H.-Y., Jang, W., Tsai, C.-L. and Lee, G.: A numerical simulation of a strong windstorm event in the Taebaek Mountain Region in Korea during the ICE-POP 2018, *Atmos. Res.*, **272**, 106158, https://doi.org/10.1016/j.atmosres.2022.106158.

Päschke, E., Leinweber, R., and Lehmann, V.: An assessment of the performance of a 1.5 μm Doppler lidar for operational vertical wind profiling based on a 1-year trial, *Atmos. Meas. Tech.*, **8**, 2251–2266, https://doi.org/10.5194/amt-8-2251-2015, 2015.

Reed, T. R.: GAP WINDS OF THE STRAIT OF JUAN DE FUCA. *Mon. Wea. Rev.*, **59**, 373–376, https://doi.org/10.1175/15200493(1931)59<373:GWOTSO>2.0.CO;2, 1931.

Ryzhkov, A., Zhang, P., Reeves, H., Kumjian, M., Tschallener, T., Trömel, S., and Simmer, C.: Quasi-Vertical Profiles—A New Way to Look at Polarimetric Radar Data. *J. Atmos. Oceanic Technol.*, **33**, 551–562, https://doi.org/10.1175/JTECH-D-15-0020.1, 2016.

Tsai, C., Kim, K., Liou, Y., Lee, G., and Yu, C.: Impacts of Topography on Airflow and Precipitation in the Pyeongchang Area Seen from Multiple-Doppler Radar Observations. *Mon. Wea. Rev.*, **146**, 3401–3424, https://doi.org/10.1175/MWR-D-17-0394.1, 2018.

Tsai, C.-L., Kim, K., Liou, Y.-C., Kim, J.-H., Lee, Y., and Lee, G.: Orographic-induced strong

https://doi.org/10.5194/amt-2022-218
Preprint. Discussion started: 1 August 2022

wind associated with a low-pressure system under clear-air condition during ICE-POP 2018, *J. Geophys. Res. Atmos.*, **127**, e2021JD036418. https://doi.org/10.1029/2021JD036418, 2022.

Tseng, Y., and Ferziger, J.: A ghost-cell immersed boundary method for flow in complex geometry. *J. Comput. Phys.*, **192**, 593–623, https://doi.org/10.1016/j.jcp.2003.07.024. 2003.

Yu, C., and Tsai, C.-L.: Surface Pressure Features of Landfalling Typhoon Rainbands and Their Possible Causes. *J. Atmos. Sci.*, **67**, 2893–2911, https://doi.org/10.1175/2010JAS3312.1, 2010.

Yu, C.-K., & Tsai, C.-L. : Structural and surface features of arc-shaped radar echoes along an outer tropical cyclone rainband. *J. Atmos. Sci.*, **70**, 56– 72. https://doi.org/10.1175/JAS-D-12-090.1, 2013.

Yu, C.-K., and Tsai, C.-L.: Structural changes of an outer tropical cyclone rain band encountering the topography of northern Taiwan. *Q. J. R. Meteorol. Soc*, **143**, 1107–1122. https://doi.org/10.1002/qj.2994, 2017.

Yu, C.-K., Cheng, L.-W., Wu, C.-C., and Tsai, C.-L.: Outer Tropical Cyclone Rainbands Associated with Typhoon Matmo (2014). *Mon. Wea. Rev.*, **148**, 2935–2952, https://doi.org/10.1175/MWR-D-20-0054.1, 2020.